Sector-zoned clinopyroxene as a recorder of magma history, eruption triggers, and ascent rates

Teresa Ubide [a,*], Silvio Mollo [b,c], Jian-xin Zhao [a], Manuela Nazzari [c]
Piergiorgio Scarlato [c]

[a] *School of Earth and Environmental Sciences, The University of Queensland, Brisbane, QLD 4072, Australia*
[b] *Department of Earth Sciences, Sapienza – University of Rome, P. le Aldo Moro 5, 00185 Roma, Italy*
[c] *Istituto Nazionale di Geofisica e Vulcanologia – INGV, Via di Vigna Murata 605, 00143 Roma, Italy*

Abstract

Sector-zoned clinopyroxene is common in igneous rocks, but has been overlooked in the study of magmatic processes. Whilst concentric zoning is commonly used as a record of physicochemical changes in the melt feeding crystal growth, clinopyroxene is also highly sensitive to crystallisation kinetics. In sector-zoned crystals, the fidelity of compositional changes as recorders of magma history is dubious and the interplay between thermodynamic and kinetic controls remains poorly understood. Here we combine electron probe and laser ablation micro-chemical maps of titanaugite crystals from Mt. Etna (Sicily, Italy) to explore the origin of sector zoning at the major and trace element levels, and its implications for the interpretation of magmatic histories. Elemental maps afford the possibility to revisit sector zoning from a spatially controlled perspective. The most striking observation is a clear decoupling of elements into sectors vs. concentric zones within single crystals. Most notably, Al-Ti enrichments and Si-Mg depletions in the prism sectors {1 0 0}, {1 1 0} and {0 1 0} relative to the hourglass (or basal) sectors {−1 1 1} correlate with enrichments in rare earth elements and highly charged high field strength elements due to cation exchanges driven by kinetic effects. In contrast, transition metals (Cr, Ni, Sc) show little partitioning into sectors and strong enrichments in concentric zones following resorbed surfaces, interpreted as evidence of mafic recharge and magma mixing. Our results document that kinetic partitioning has minor effects on the compositional variations of cations with low charge relative to the ideal charge/radius of the structural site they occupy in the clinopyroxene lattice. We suggest that this may be due to a lower efficiency in charge balance mechanisms compared to highly charged cations. It follows that compatible metals such as Cr can be considered trustworthy recorders of mafic intrusions and eruption triggers even in sector-zoned crystals. We also observe that in alkaline systems where clinopyroxene crystallisation takes place at near-equilibrium conditions, sector zoning should have little effect on Na-Ca partitioning and in turn, on the application of experimentally calibrated thermobarometers. Our data show that whilst non-sector-zoned crystals form under relatively stagnant conditions, sector zoning develops in response to low degrees of undercooling, such as during slow magma ascent. Thus, we propose that the chemistry of sector-zoned crystals can provide information on magma history, eruption triggers, and possibly ascent rates.

* Corresponding author.
E-mail address: t.ubide@uq.edu.au (T. Ubide).

1. INTRODUCTION

Compositional zoning in igneous minerals is increasingly exploited as an archive of magmatic histories. Mineral records have guided improved reconstruction of magma plumbing systems and better understanding of the processes, depths and timescales that lead to volcanic eruptions (e.g., Davidson et al., 2007; Putirka, 2008; Costa and Morgan, 2011; Ganne et al., 2018; Ubide and Kamber, 2018). An emerging discussion point is constraining what exactly each mineral is able to record in its chemical stratigraphy, and for how long such records are maintained. Different minerals have distinct textural and compositional responses to physicochemical changes in the magmatic environment (e.g., Ubide and Kamber, 2018) and the rate of diffusion of chemical species in crystal lattices has a strong role in the preservation or resetting of compositional zoning during magma storage at high temperature (e.g., Bouvet de Maisonneuve et al., 2016).

Clinopyroxene is a common early crystallising mineral in mafic to intermediate magmas and crystallises across a wide range of pressures and water contents (Armienti et al., 2007, 2013; Putirka, 2008). It is sensitive to pressure, temperature, water content and magma composition (e.g., Putirka, 2008; Perinelli et al., 2016; Mollo et al., 2015, 2018) and is characterised by relatively slow lattice diffusion (Van Orman et al., 2001; Costa and Morgan, 2011; Müller et al., 2013), thus holding a protracted record of pre-eruptive processes (Ubide and Kamber, 2018). Recently, clinopyroxene zoning has been shown to be particularly useful to track the intrusion of mafic magma into plumbing systems, constrain the effectiveness of magma recharge as an eruption trigger, and to calculate typical time windows from recharge to eruption (Ubide and Kamber, 2018; Petrone et al., 2018). However, experimental petrology studies highlight that clinopyroxene compositions do not only respond to thermodynamic conditions, but also to kinetic effects during crystal growth (Kouchi et al., 1983; Hart and Dunn, 1993; Skulski et al., 1994; Lofgren et al., 2006; Schwandt and McKay, 2006; Mollo et al., 2013). Indeed, crystal growth is halted when local equilibrium is established at the crystal-melt interface under steady-state regimes. A certain amount of undercooling (difference between the liquidus temperature and the system temperature: $\Delta T = T_{liquidus} - T_{crystallisation}$; cf. Mollo and Hammer, 2017) is always necessary for the crystals to grow to the size of phenocrysts. In natural volcanic rocks, augite crystals often deviate from the frequently assumed 'tree-ring' model and develop sector zoning (Hollister and Gancarz, 1971; Arculus, 1973; Ferguson, 1973; Downes, 1974; Leung, 1974; Dowty, 1976; Duncan and Preston, 1980; Shimizu, 1981; Watson and Liang, 1995; Brophy et al., 1999; Hammer et al., 2016; Welsch et al., 2016; Neave and Putirka, 2017; Mollo and Hammer, 2017; Stock et al., 2018), generating an hourglass form (Fig. 1). At a given stage of crystal growth, sector-zoned crystals may grow with different chemistries along different crystallographic orientations, even if the melt composition, pressure, temperature and water content remain constant (e.g., Nakamura, 1973; Mollo and Hammer, 2017). Hence,
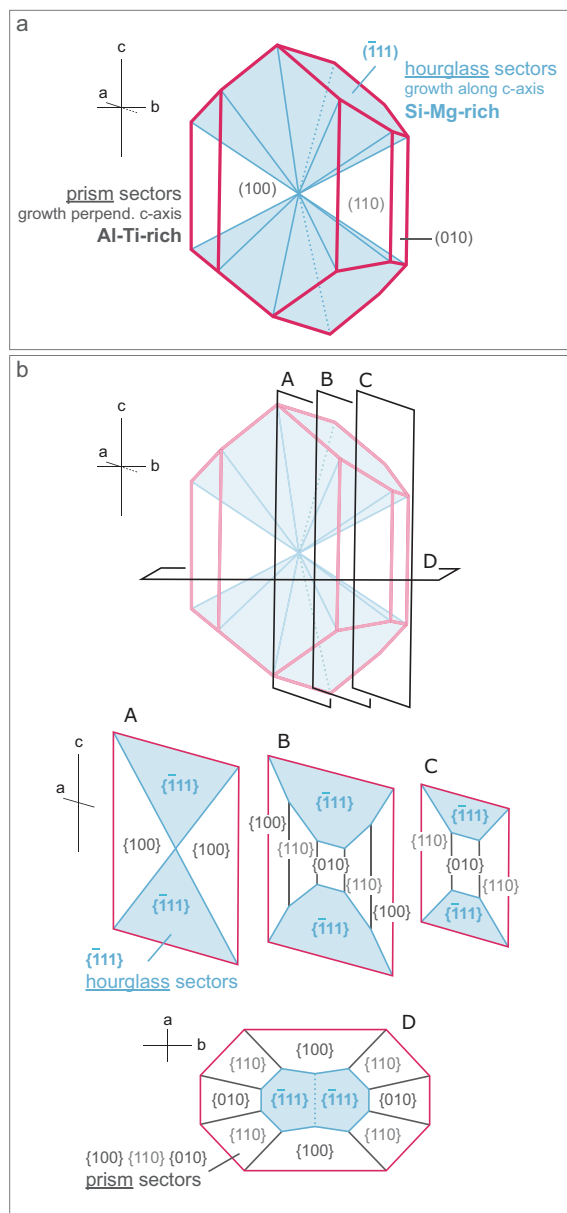

Fig. 1. Sector-zoned clinopyroxene model. (a) 3D morphological model of titanaugite, composed of 12-pyramid sectors that meet at the centre of the crystal: 2x {1 0 0} sectors + 4x {1 1 0} sectors + 2x {0 1 0} sectors + 4x {−1 1 1} sectors = 12 sectors in total. Sector-zoned crystals comprise two types of sectors: hourglass (or basal), and prism. The hourglass or basal form {−1 1 1}, highlighted in blue, grows along the c-axis and is rich in Si and Mg relative to the prism forms {1 0 0}, {1 1 0} and {0 1 0}, which grow perpendicular to the c-axis and have relatively higher concentrations of Al and Ti. (b) Hypothetical 2D cuts of the crystal in different orientations, along the a- and c-axes (cut A through the centre of the crystal; cuts B–C off-centre) and along the a- and b-axes (cut D perpendicular to the c-axis, and off-centre). Cuts along the c-axis show hourglass sectors at both ends, whereas cuts perpendicular to the c-axis show hourglass sectors in the centre surrounded by prism sectors. Modified from Leung (1974). Note that the model assumes full crystallisation in sectors, but sector-zoned crystals can mantle non-sector zoned cores, and be overgrown by distinct rims. (For interpretation of the references to colour in this figure legend, the reader is referred to the web version of this article.)

a key question arises: can we assess which chemical elements, if any, are trustworthy recorders of magma histories?

Answering this question requires evaluation of local equilibrium between the different sectors and the melt and, ultimately, a better understanding of the mechanisms and consequences of sector zoning in igneous minerals. Early petrographic and electron microprobe studies on sector-zoned titanaugite observed that the prism sectors {1 0 0}, {1 1 0} and {0 1 0}, which grow perpendicular to the *c* crystallographic axis, have a deeper colour than the hourglass basal sectors {−1 1 1}, which grow faster along the c-axis (Wass, 1973; Leung, 1974; Downes, 1974; Fig. 1); the deeper colour of prism sectors was ascribed to higher concentrations in Ti and Al compared to hourglass sectors, which were relatively enriched in Si and Mg. These coupled variations were related to charge-balancing mechanisms, as increased substitution of Si^{4+} for Al^{3+} in tetrahedral sites requires incorporation of highly charged cations such as Ti^{4+} in M1 octahedral sites typically occupied by Mg^{2+} or Fe^{2+}. The occurrence of sector zoning was discussed in terms of the kinetics of attachment of cations to crystallographic faces with different site arrangements (Ferguson, 1973; Nakamura, 1973; Dowty, 1976) and growth rates relative to diffusion in the melt boundary layer adjacent to the advancing crystal sectors (Downes, 1974; Leung, 1974). Later, experimental data demonstrated that sector zoning is strongly controlled by the degree of magma undercooling and, in turn, by the crystal growth rate (Kouchi et al., 1983).

With the advent of *in situ* trace element analysis by ion microprobe, several studies (mostly experimental) reported sector zoning of Cr, Sc, V, Li, Rare Earth Elements (REE) and High Field Strength Elements (HFSE), independent of compatible/incompatible behaviour in clinopyroxene (Shimizu, 1981; Hart and Dunn, 1993; Skulski et al., 1994; Lofgren et al., 2006; Schwandt and McKay, 2006). These studies, however, reported inconsistent partitioning of trace elements with respect to prism vs. hourglass sectors and, to the best of our knowledge, trace element sector zoning remained underexplored in natural samples. The sector zoning debate was recently reinvigorated with original textural observations, major element analyses and thermobarometric estimates on Hawaiian clinopyroxenes by Hammer et al. (2016) and Welsch et al. (2016). These authors proposed that sector zoning is related to diffusion-controlled dendritic growth under conditions of high undercooling. The results also evidenced the need for high-resolution textural and compositional investigations to evaluate kinetic and thermodynamic conditions of crystallisation, before extracting interpretations on magma history.

Here we tackle fundamental understanding of sector zoning by investigating titanaugite crystals in basaltic products of recent eruptions at Mt. Etna (Sicily, Italy) with *in situ* quantitative analysis and mapping of major and trace elements. The rocks are alkaline trachybasalts from eruptions in 1974 and 2002–03 (e.g., Andronico et al., 2005; Corsaro et al., 2009; Ubide and Kamber, 2018) and they have relatively simple mineral assemblages, including titanaugite crystals that are sector-zoned with a relatively small size, enabling time-efficient *in situ* determinations. High-resolution compositional mapping affords visualisation and modelling of major and trace element zoning at the micrometre scale, providing a new opportunity to investigate and establish reliable indicators of magmatic processes in sector-zoned crystals.

2. MATERIAL AND METHODS

We investigate sector-zoned titanaugite crystals from the so-called 'eccentric' or 'deep-dyke-fed' flank eruptions at Mt. Etna, which tap deep, undegassed magmas through pathways that bypass the central conduits of the volcano, generating monogenetic volcanism (Behncke and Neri, 2003; Clocchiatti et al., 2004; Métrich et al., 2004; Corsaro et al., 2009). We focus on crystals in lava flow and bomb samples from eruptions in 1974 (southwest flank eruption; Tanguy and Kieffer, 1976; Corsaro et al., 2009) and 2002–03 (south flank eruption; Clocchiatti et al., 2004; Andronico et al., 2005). The samples are a sub-set from a study focused on oscillatory zoned crystals, where sector-zoned crystals were intentionally avoided (Ubide and Kamber, 2018).

The rocks are vesicular and variably porphyritic trachybasalts, with phenocrysts of clinopyroxene and minor olivine dispersed in a finely crystalline to glassy groundmass. Titanomagnetite is a frequent inclusion in the phenocrysts and plagioclase is restricted to the groundmass, as is typical in deep-dyke fed, undegassed eccentric magmas (e.g., Corsaro et al., 2009). Clinopyroxene phenocrysts from the 1974 eruption range in size from 200 μm to >1 mm and make up <5 vol.% of the rock. They have polyhedral morphologies (as opposed to dendritic shapes, which are not observed) and often occur within glomerocrysts. Crystals from the 2002–03 eruption are also euhedral but significantly larger (typically isolated crystals several mm in size) and more abundant (10–20 vol.%). Petrography and preliminary analysis informed the selection of 9 titanaugite crystals from 6 samples, with a variety of zoning patterns of particular interest for detailed chemical study (Supplementary Table 1). Sectors were identified using theoretical cuts across a 12-pyramid morphological model of titanaugite (Fig. 1), following the pioneering work of Leung (1974) and Downes (1974).

Major element compositions were determined by electron probe microanalysis (EPMA) in May-June 2017 at INGV Rome, using a JEOL JXA-8200 instrument equipped with five wavelength dispersive spectrometers. Analyses were performed on carbon-coated thin sections under high vacuum conditions using an accelerating voltage of 15 kV and an electron beam current of 7.5nA, with a beam diameter of 2.5 μm. Elemental counting times were 10 s on the peak and 5 s on each of two background positions, except for chromium, which was measured for 20 s on the peak and 10 s on each background position. Corrections for inter-elemental effects were made using a ZAF (Z: atomic number; A: absorption; F: fluorescence) procedure. Calibration used a range of standards from Micro-Analysis Consultants (MAC; http://www.macstandards.co.uk):

albite (Si-PET, Al-TAP, Na-TAP), forsterite (Mg-TAP), augite (Fe-LIF), apatite (Ca-PET), orthoclase (K-PET), rutile (Ti-PET), rhodonite (Mn-LIF) and JEOL Cr metal (Cr-PET). Spot analyses defined transects across the crystals with constant spot separation, typically of 5 μm. Results were screened based on stoichiometry and analytical totals, and the final dataset comprises 1595 analyses (Supplementary Table 2). Smithsonian augite (Jarosewich et al., 1980) and MAC augite were used as quality monitor standards and for the calculation of accuracy and precision. Accuracy was better than 1–5% except for elements with abundances below 1 wt.%, for which accuracy was better than 5–10%. Precision was typically better than 1–5% for all analysed elements. For mapping, we used 0.5 μm pixel size and 50–150 ms dwell time per pixel, measuring up to 5 elements per analysis (one per diffracting crystal). Mapped areas varied in size from 405 × 275 μm to 512 × 512 μm, with total experiment times of 7–24 h.

Trace element zoning was investigated using laser ablation inductively coupled plasma mass spectrometry (LA-ICP-MS) mapping, following the rastering technique described in Ubide et al. (2015). The experiments were carried out in August-November 2017 at The University of Queensland Centre for Geoanalytical Mass Spectrometry, Radiogenic Isotope Facility (UQ RIF-lab). We used an ASI RESOlution 193 nm excimer UV ArF laser ablation system with a dual-volume Laurin Technic ablation cell and GeoStar Norris software, coupled to a Thermo iCap RQ quadruple mass spectrometer with Qtegra software. Ablation was performed in ultrapure He to which Ar make-up gas with a trace amount of N_2 was added for efficient transport and to aid ionisation. Two experiments were run per crystal with identical laser parameters and different analyte menus to obtain maps on a large number of trace elements without compromising spatial resolution (see Ubide et al., 2015). Details of laser parameters, gas flows, and mass spectrometer operation are given in Supplementary Table 3. The instruments were tuned with scans on NIST612 glass reference material. Elemental maps were built with Iolite (Paton et al., 2011) v2.5 in quantitative mode, using NIST610 glass reference material as the calibration standard and calcium concentrations previously obtained by electron microprobe (22.2 ± 0.5 wt.% CaO; n = 1595) as internal standard. Accuracy and precision were monitored using BHVO-2G, BCR-2G and BIR-1G glass reference materials as secondary standards (http://georem.mpch-mainz.gwdg.de/). Precision was better than 5% and accuracy was better than 5–15% except for Ti; this element was measured using mass 48 (^{48}Ti) and returned values 30–60% below preferred values on BHVO-2G, BCR-2G and BIR-1G due to the sulphur-based polyatomic interference $^{32}S^{16}O$ on the calibration standard NIST610 (ca. 600 ppm S). Note however that Ti concentrations were analysed reliably by electron microprobe as detailed above. Limits of detection (Longerich et al., 1996) were typically at the sub-ppm level for most analysed elements and below 5 ppm for Al and Cr.

Following visual examination of zoning on LA-ICP-MS maps, the Monocle add-on for Iolite (Petrus et al., 2017) was used to extract average compositions for crystal zones (Supplementary Table 4). This approach provides high-precision compositional data by averaging large signals pooled from compositionally homogeneous regions (zones), rather than local compositions obtained with classic spot analyses, which also pose potential downhole-fractionation effects (Petrus et al., 2017). Regions of interest were defined following zoning in Zr and Ce (sector zones) as well as Cr (concentric zones), using 'From selections' as input map type. We defined several polygons per zone and results with the lowest standard deviations and smoothest REE-normalised patterns were selected to ensure the representativeness of averaged concentration values and avoid user bias. In addition, we extracted compositional profiles across sectors following the same transects analysed by EPMA, using the CellSpace module in Iolite (Paul et al., 2012) (Supplementary Table 5).

3. RESULTS

3.1. Hourglass zoning along the c-axis

We first consider a relatively simple example of sector zoning where the crystal is cut along the *c* and *a* crystallographic axes, so that the {−1 1 1} and {1 0 0} sectors meet at a central point (cut A in Fig. 1; major and trace element results in Figs. 2–4). Sector zoning is evident upon examination under transmitted light and backscattered electron imaging (Fig. 2). In addition, there is an irregular concentric zone where the sectoring angles change slightly, suggesting a change in environmental conditions (Fig. 2). Major element maps and traverses reveal sharp enrichments in Si-Mg in the hourglass basal sectors {−1 1 1}, whereas the prism sectors {1 0 0} are enriched in Al-Ti-Fe (total iron as Fe^{2+}) (Figs. 2 and 3). The irregular concentric zone has a relatively uniform composition across sectors and is enriched in Si-Mg and depleted in Al-Ti-Fe relative to regular sector compositions (Fig. 2). This zone also shows a clear uptake in Cr that is resolvable by electron microprobe analysis (Fig. 3), indicating a reheating event related to mafic recharge (Streck, 2008; Ubide and Kamber, 2018). The Na and Ca profiles are virtually flat, with no observable partitioning into sectors and no variations in relation to mafic recharge (Fig. 3).

LA-ICP-MS maps reveal striking decoupling of trace elements into sector vs. concentric zones (Fig. 4). Incompatible elements, including REE and HFSE, show clear sector partitioning following the Al pattern, as well as small depletions along the recharge zone. In contrast, Cr, Ni and to a lesser extent Sc, as compatible transition metals (D_{Cr} = >3–17, D_{Ni} = 2.8–3.9 and D_{Sc} = 5.8–8.5; mineral/melt partition coefficients for Etnean lavas reported in D'Orazio et al., 1998), show sharp enrichments along the recharge zone, and only minor sectoral variations (Fig. 4). The decoupling is not, however, purely related to compatible/incompatible behaviour. Vanadium for example, is mildly compatible (D_V = 1.3–1.8; D'Orazio et al., 1998) in the clinopyroxene lattice but shows predominant partitioning into sectors. Incompatible Li, on the other hand, shows low concentrations that are homogeneously distributed across the crystals.
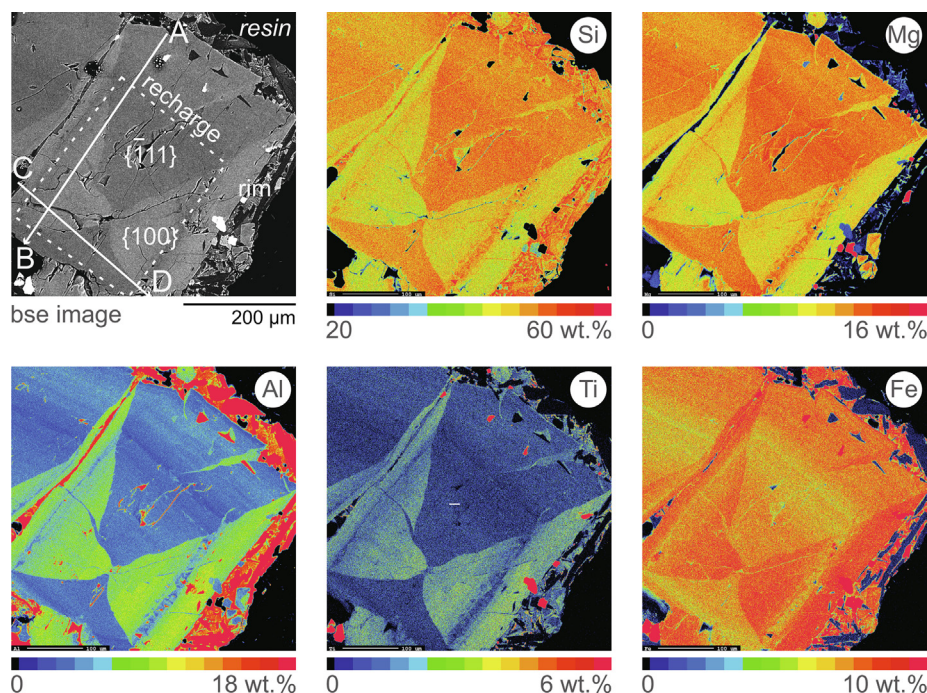
Fig. 2. Back-scattered electron (bse) image and major element maps of titanaugite 15RC018_Cpx1 (centre) and part of titanaugite 15RC018_Cpx2 (top left corner), obtained by electron microprobe. These sections cut through the centre of the crystals, similar to section A in Fig. 1b. The hourglass form {−1 1 1}, growing along the *c* crystallographic axis, is enriched in Si-Mg and depleted in Al-Ti-Fe relative to form {1 0 0}, growing perpendicular to the *c* axis. The dashed white line marks a mafic recharge zone, slightly corroded and enriched in Mg and transition metals (see also Fig. 4). White arrows mark the location of two transects AB and CD across crystal 15RC018_Cpx1, presented in Fig. 3 (data in Supplementary Table 2). The crystals are part of a glomerocryst composed of titanaugite and olivine, embedded in a hypocrystalline groundmass with microcrysts of plagioclase, clinopyroxene, olivine, titanomagnetite, and glass.

A pattern emerges when zoning is examined from a crystal-chemical point of view, considering the charge of cations and their site occupancy into M1 octahedral sites (predominantly occupied by Mg^{2+} in VI-fold coordination) and M2 distorted octahedral sites (larger and primarily occupied by Ca^{2+} in VIII-fold coordination) (e.g., Morimoto et al., 1988; Wood and Blundy, 2003). In M1 sites, highly charged cations such as the tetravalent and pentavalent HFSE (e.g., Zr^{4+} and Nb^{5+}) are enriched in prism sectors {1 0 0} over hourglass basal sectors {−1 1 1}, whereas cations with lower charge (e.g., Cr^{3+} and Ni^{2+}) show sharp enrichments along the recharge zone. In M2 sites, trivalent lanthanides (e.g., REE^{3+}, Y^{3+}) are predominantly sector-zoned, confirming that charge balancing mechanisms are key controls on sector zoning (see following Discussion).

3.2. Variations amongst sectors perpendicular to the c-axis

Similarly oriented crystal-cuts (parallel to c-a-axes), but off-centre (cuts B and C in Fig. 1) show the hourglass basal sectors {−1 1 1} in contact with several or all of the prism sectors, {0 1 0}, {1 1 0} and {1 0 0} towards the crystal margin (Fig. 5). Compositional variations amongst prism sectors, all growing perpendicular to the c-axis, are minor compared to the marked difference they show relative to the hourglass sector growing along the c-axis. Nevertheless, sector {1 0 0} is most different from {−1 1 1}, whereas

{1 1 0} and {0 1 0} show intermediate compositions. Differential partitioning amongst prism sectors seems to be restricted to highly charged elements such as Ti and Zr. Concentrations are virtually identical for Ca and Na. The example crystal in Fig. 5 includes a well-developed, wavy concentric zone crosscutting the hourglass basal sectors {−1 1 1} as well as prism sectors {1 1 0}, resulting in an off-set and change in angle of the common boundary. The wavy surface suggests crystal dissolution and is followed by a distinctly Cr-rich, mafic composition, most clearly resolved by LA-ICP-MS mapping. The Cr enrichment is accompanied by enrichments in Ni and Sc and depletions in REE and HFSE, in agreement with the mafic recharge pattern observed for the crystals in Figs. 2–4. Additionally, LA-ICP-MS mapping reveals a further Cr-rich zone closer to the centre of the crystal that, in turn, is not related to an obvious textural change.

3.3. General compositional variations

Taken as a whole, sector zoning data from crystals cut in different orientations show systematic compositional variations: {1 0 0} < {1 1 0} ≤ {0 1 0} << {−1 1 1} in Si and Mg, together with opposite variations in Al, Ti and to a lesser extent Fe^{3+} (Fig. 6; Table 1). Major element differences between {1 0 0} and {−1 1 1} can be as large as 6 wt.% SiO_2, 4 wt.% MgO and Al_2O_3, and up to 2 wt.% TiO_2 and total iron as FeO. Concentrations of CaO are virtually
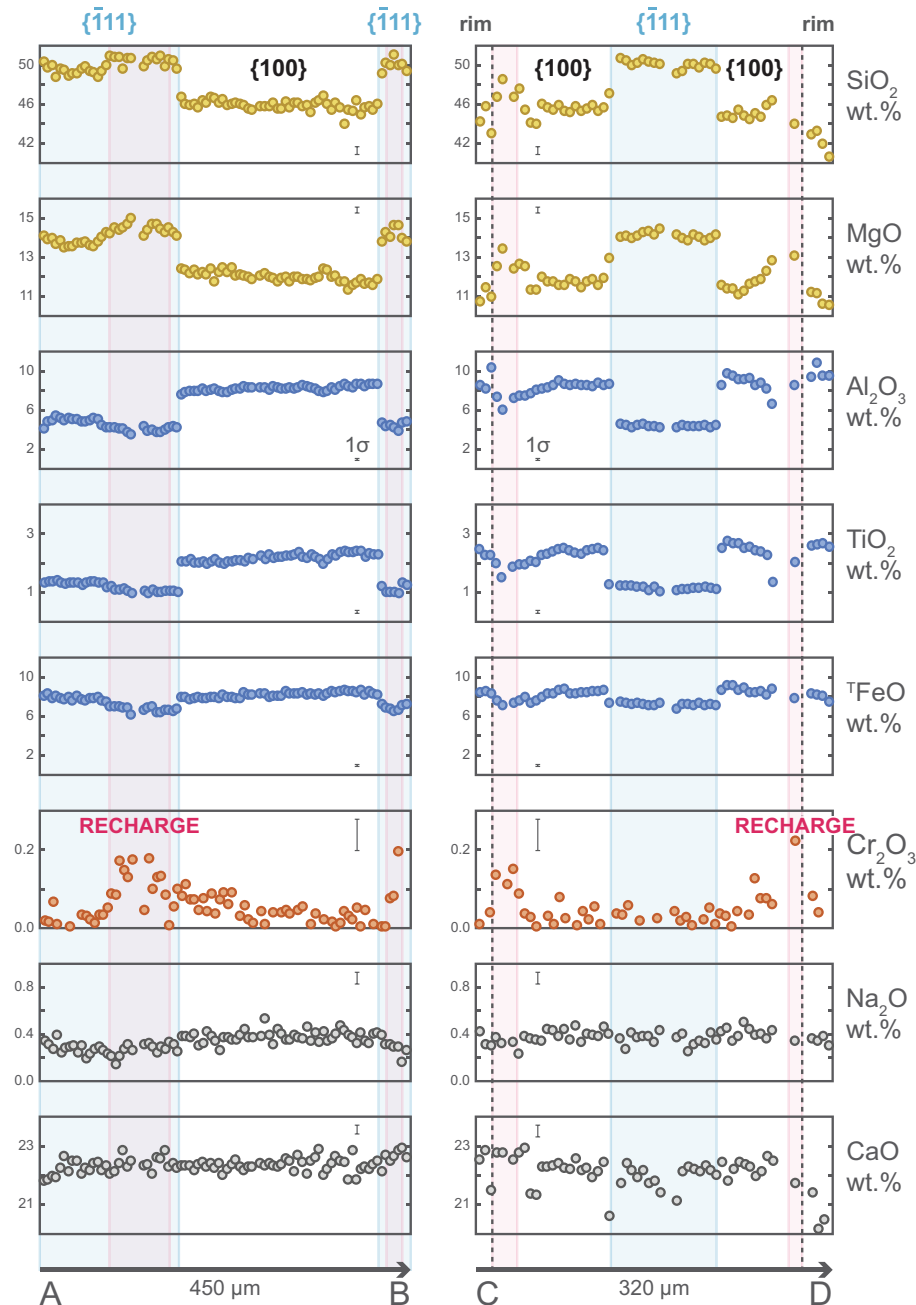
Fig. 3. Electron microprobe transects across titanaugite 15RC018_Cpx1. The location of the transects (AB and CD) is marked in Fig. 2. Each spot analysis is separated by 5 μm, excepting spots screened out or with concentrations below detection limits. Spots on the hourglass form $\{-1\,1\,1\}$ have blue background and are characterised by high concentrations of Si-Mg and low concentrations of Al-Ti-Fe. Spots on the mafic recharge zone have pink background and are characterised by high concentrations of Mg and particularly Cr (above the limit of detection). Note the presence of a final growth zone (rim) characterised by high Al-Ti and low Mg-Cr contents on either side of transect CD, marked with black dashed lines; the rim was not detected in transect AB. The concentrations of Na and Ca are relatively constant across both transects, independent of both sector and oscillatory zoning. ^{T}FeO is total iron as FeO. One standard deviation error bars are shown but other than for Cr_2O_3 they are similar to or smaller than symbols. (For interpretation of the references to colour in this figure legend, the reader is referred to the web version of this article.)

identical across sectors and variations in Na_2O are very subtle to non-resolvable (Na_2O apparently increases by ca. 0.1 wt.% from $\{-1\,1\,1\}$ to $\{1\,0\,0\}$; Figs. 3 and 5). Sector zoning has a major effect on the partitioning of most trace elements, which follow the incorporation of Al and Ti. Concentrations of REE^{3+}, Y^{3+}, Zr^{4+}, Hf^{4+} and V^{4+} in $\{1\,0\,0\}$ are typically double those in $\{-1\,1\,1\}$, and are up to five times greater in highly charged cations Nb^{5+} and
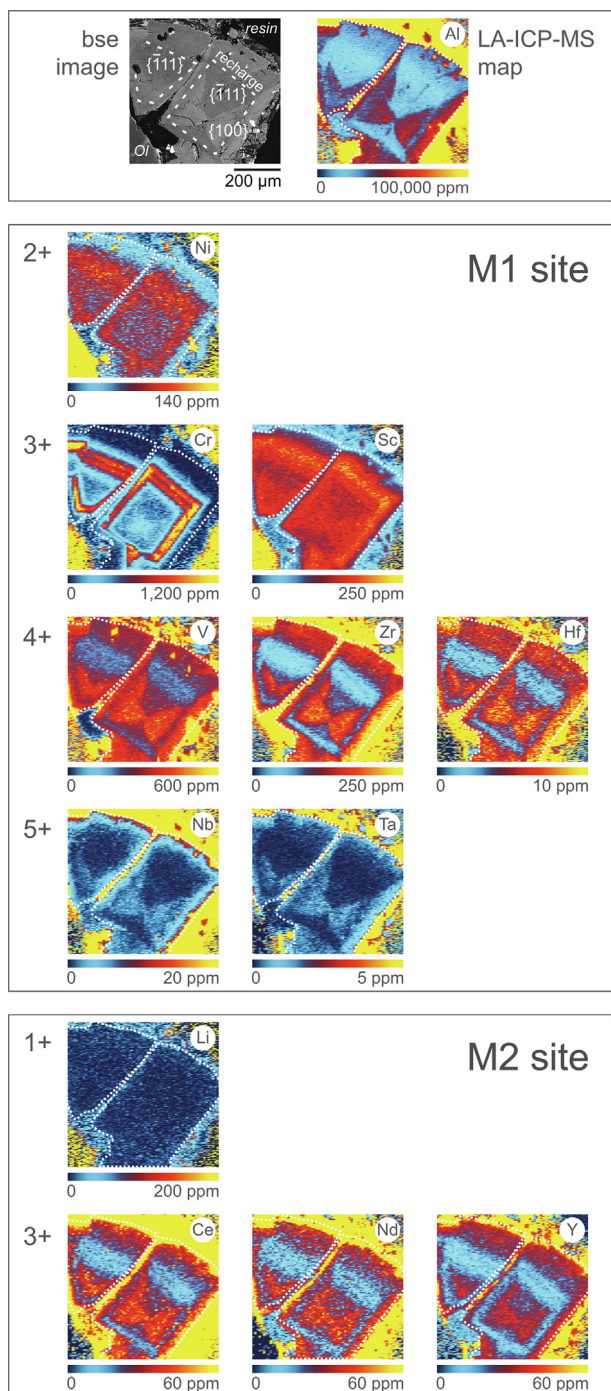
Fig. 4. Minor and trace element maps of titanaugite 15RC018_Cpx1 (centre) and titanaugite 15RC018_Cpx2 (left), obtained by LA-ICP-MS. The top panel provides crystallographic and petrographic context on a back-scattered electron image (bse image: Ol – olivine; resin – epoxy at the edge of the thin section) and a LA-ICP-MS aluminium map. Trace elements are grouped based on the cation site in which they partition (octahedral sites M1 and M2) and on the cation charge (1+ to 5+). Strikingly, low-charge transition metals such as Ni, Cr and Sc are enriched along a mafic recharge zone, whereas high-charge incompatible trace elements show sector zoning with a pattern similar to Al. The dotted white lines mark the outlines of the crystals.

Ta^{5+} (Fig. 7; Supplementary Table 4). In contrast, low-charge M1 cations Ni^{2+}, Cr^{3+} and Sc^{3+} show little sector partitioning, and the ratios between elemental concentrations in {1 0 0} relative to {−1 1 1} are close to unity (1 ± 0.3; Fig. 7). Notably, for trace cations hosted in the M1 crystallographic site, the {1 0 0}/{−1 1 1} enrichment factor correlates positively with the ionic potential (Z/r^2, where Z is the charge of a cation with ionic radius r).

Concentric enrichments in transition metals Ni, Cr and Sc are observed in seven of the nine crystals analysed (Supplementary Table 1). Consistently, high-Cr-Ni-Sc zones are relatively depleted in REE and HFSE, and overgrow dissolution surfaces suggesting mixing with hotter, more primitive magma. Chromium enrichments in particular are even detectable with electron microprobe (Figs. 3, 5, 8) and correlate positively with MgO within each sector group (Fig. 6). Interestingly, not all Cr-rich layers show sharp Mg enrichments, as zoning of divalent Mg-Fe in the inner parts of crystals may be smoothed by diffusion during storage at high temperature (Nakagawa et al., 2002; Ubide and Kamber, 2018). When coupled to major element variations, high-Cr zones are enriched in Si-Mg and depleted in Al-Ti-Fe with relative variations of 0.5–2 wt.% oxide concentrations compared to regular sector compositions (Fig. 3).

Four of the crystals have outermost rims that show systematic enrichments of 1–2 wt.% Al_2O_3 and 0.5 wt.% TiO_2 relative to the composition they overgrow (Figs. 3, 6; Supplementary Tables 1 and 2). Progressive enrichments in Al-Ti are typical of crystallisation under increasing magma cooling and crystal growth rates (Mollo et al., 2013), which are likely related to magma ascent towards the surface (Ubide and Kamber, 2018).

Rounded cores with marked enrichment in Na relative to all other compositions ($+0.3$ wt.% Na_2O and -1 wt.% CaO relative to regular sector compositions, Figs. 6, 8; Supplementary Tables 1 and 2) suggest crystallisation at higher pressure (Nimis, 1995; Putirka, 2008). High-Na cores, observed in four of the crystals, are typically anhedral with irregular morphologies at the contact with sector-zoned mantles, which begin with a Cr-rich zone (Fig. 8). These observations suggest partial dissolution of the cores prior to crystallisation of the mantles from more mafic magma. The cores may show complex zoning involving concentric variations as well as resorption surfaces. However, sector zoning within cores was not observed.

4. DISCUSSION

4.1. Origin of sector zoning

Over the past 50 years, several crystallographic and thermodynamic models have attempted to explain the fundamental mechanisms behind sector zoning (a comprehensive review can be found in Schwandt and McKay, 2006). Early crystallographic studies on clinopyroxene noted the preferential uptake of elements in crystal faces with different geometric arrangements of T-M1-M2 sites (Ferguson, 1973; Nakamura, 1973; Dowty, 1976). Meanwhile, empirical studies suggested the role of differential growth rates along the c (fastest) >> b (intermediate)
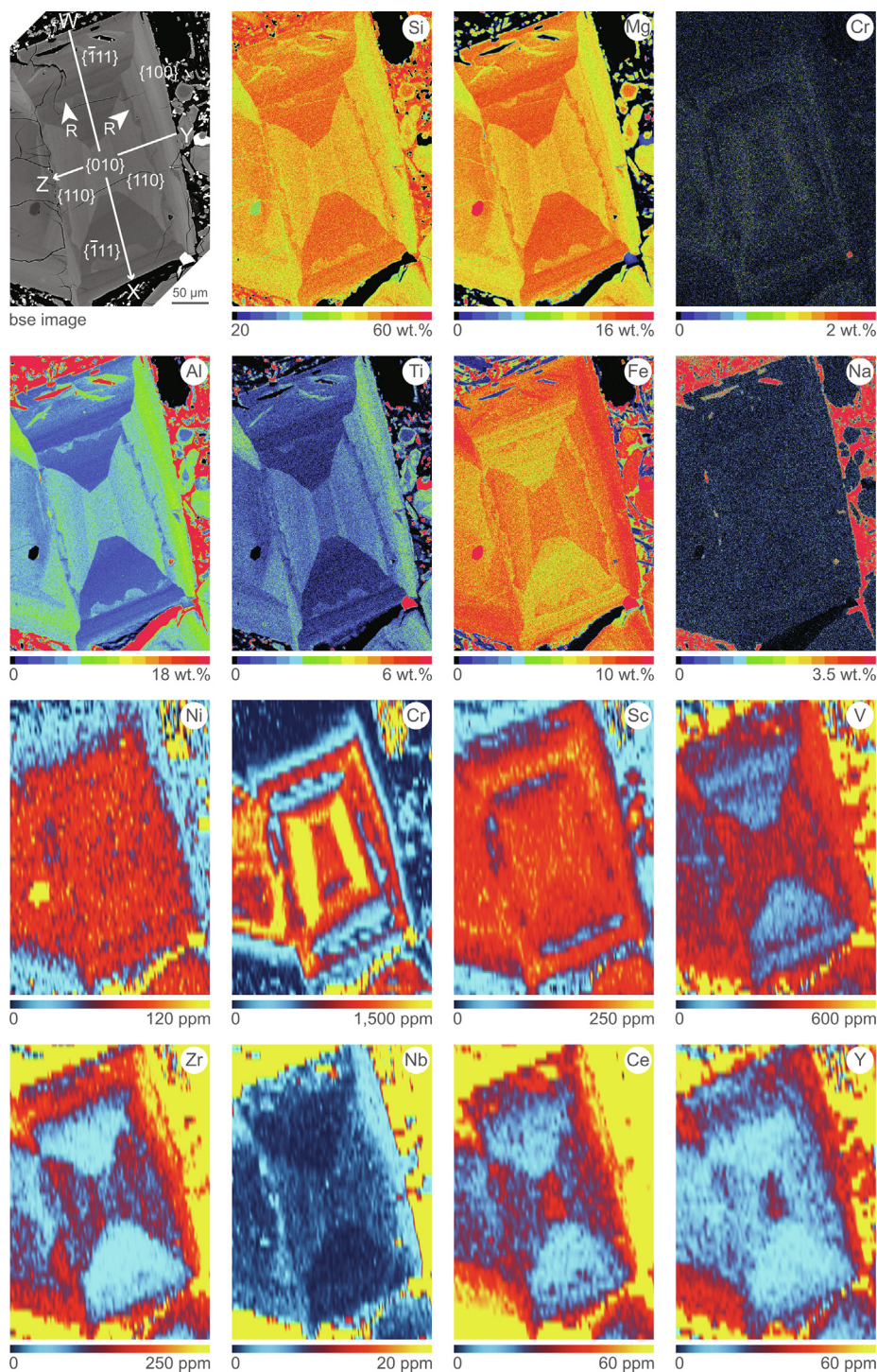
Fig. 5. Major and trace element maps of titanaugite 15RC013_Cpx2, obtained by electron microprobe (top two rows) and LA-ICP-MS (bottom two rows). The back-scattered electron (bse) image provides context. The crystal (cut B to C in Fig. 1b) belongs to a glomerocryst set in a hypocrystalline groundmass. The hourglass form $\{-1\ 1\ 1\}$, growing along the c crystallographic axis, is enriched in Si-Mg and depleted in Al-Ti-Fe-V-HFSE-REE relative to forms $\{0\ 1\ 0\}$, $\{1\ 1\ 0\}$ and $\{1\ 0\ 0\}$, growing perpendicular to the c axis. The white arrows 'R' mark a mafic recharge zone, generating an irregular dissolution surface and further crystal growth with high concentrations in Mg and transition metals. There is no significant zoning in Na. Spot analyses along traverses W-X and Y-Z are available in Supplementary Table 2.

$> a$ (slowest) crystallographic axes relative to diffusion rates of cationic species in the melt (Downes, 1974; Leung, 1974). Kinetic effects were explored further in later experimental investigations, where crystal growth rates were modulated as a function of undercooling (Kouchi et al., 1983; Lofgren et al., 2006; Schwandt and McKay, 2006). The
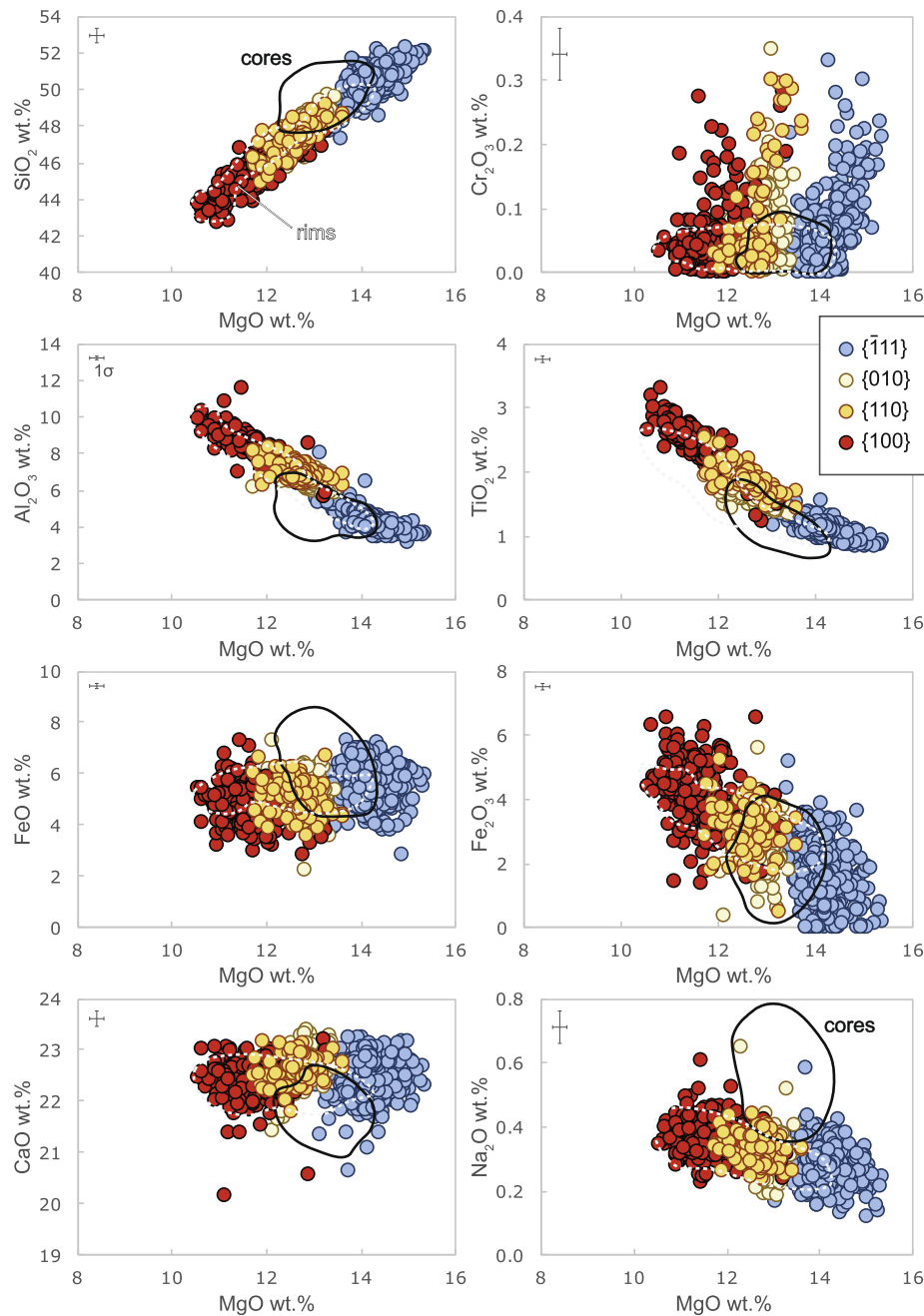
Fig. 6. Major element variations amongst sectors in clinopyroxene from the 1974 and 2002-03 eccentric eruptions at Mt. Etna (1595 data from 9 crystals in 6 samples; Supplementary Tables 1 and 2). Compositional ranges of recycled cores and outermost rims are marked with solid black and dashed light grey fields, respectively. FeO and Fe_2O_3 wt.% are calculated according to stoichiometric criteria (Droop, 1987). One standard deviation error bars are shown but other than for Cr_2O_3 and Na_2O they are similar to or smaller than symbols.

experimental perspective highlighted that sector zoning is strongly dependent on the rate at which crystals grow, and modelling of trace element data by Watson and Liang (1995) suggested that sector zoning can develop whenever the extent of crystal growth is larger than the length scale of lattice diffusion. Overall, there is general agreement that sector zoning responds to the interplay between crystallographic control intrinsic to the mineral and kinetic effects imposed by the magmatic environment (Lofgren et al., 2006; Schwandt and McKay, 2006).

However, what has been lacking in this debate is spatially resolved chemical evidence of sector zoning in natural crystals, with the aim of understanding the consequences of sector partitioning on petrogenetically relevant elements. Notable efforts in this direction include Claeson et al. (2007), who approached elemental mapping of oikocrysts from the Norra Ulvö gabbro in Sweden with individual LA-ICP-MS spot analyses, and Welsch et al. (2016), who integrated detailed textural and major element information on ankaramite clinopyroxenes from Hawaii, proposing

Table 1
Typical major and trace element compositional variations across sectors in clinopyroxene from the 1974 and 2002–03 eccentric eruptions at Mt. Etna.

Sector	Hourglass {−1 1 1}	Prism {0 1 0}	Prism {1 1 0}	Prism {1 0 0}
EPMA (wt.%)				
SiO_2	48–52	46–49	45–49	43–48
MgO	13–15	12–13	12–13	11–13
Al_2O_3	3–6	6–7	6–8	6–10
TiO_2	1–1.5	1.5	1.5–2	1.5–3
TFeO	6–8	7–8	8	8–9
Na_2O	0.1–0.4	0.2–0.4	0.2–0.4	0.2–0.4
CaO	22–23	22–23	22–23	22–23
Cr_2O_3	≤0.2	≤0.2	≤0.2	≤0.2
LA-ICP-MS (ppm)				
Li	1–4	1–2	1–5	1.5–3
Sc	110–140	130–160	130–150	130–150
V	220–240	290–330	280–350	350–380
Cr[a]	50–260	60–900	90–600	130–380
Ni	55–65	50–65	55–65	40–60
Zr	50–75	80–100	95–125	130–180
Nb	0.3–0.5	0.5–0.7	0.7–1.1	1–3
Hf	2–3.5	3.5–4.5	4–5.5	5–7
Ta	0.1	0.1	0.2–0.3	0.2–0.5
Y	14–18	19–27	18–22	20–30
La	4.5–6	6–11	7–9	10–14
Ce	16–20	21–36	25–30	30–45
Pr	3–3.5	4–6	4–5	5–7
Nd	16–19	22–34	23–28	29–38
Sm	5–6	6–9	6–8	8–11
Eu	1.5–2	2–3	2–3	2.5–3.5
Gd	4–6	6–9	6–8	8–9
Tb	0.7–0.8	0.9–1.2	0.9–1	1.1–1.3
Dy	3.5–4	4.5–7	4.5–5.5	5.5–7
Ho	0.6–0.7	0.8–1.2	0.8–1	1–1.2
Er	1–2	1.8–2.6	1.9–2.2	2.4–2.8
Tm	0.2	0.2–0.3	0.2–0.3	0.3
Yb	1.1–1.2	1.3–1.8	1.4–1.6	1.8–2
Lu	0.1–0.2	0.2	0.2	0.2–0.3

Note the strong compositional differences between hourglass and prism sectors, and the smaller, overlapping differences amongst prism sectors.

TFeO is total iron as FeO.

[a] Trace element compositions were extracted avoiding Cr-rich recharge zones as much as possible.

disequilibrium crystallisation of early dendrites followed by later sector infilling.

High-resolution chemical mapping of Etnean clinopyroxenes from this study makes it possible to link crystal textures to quantitative major and trace element variations across sectors. The geometrical perfection of crystal faces and concentric zoning from core to rim, crosscutting sector boundaries (Figs. 2, 4, 5, 8), indicate polyhedral crystallisation under conditions approaching equilibrium (e.g., Lofgren et al., 2006). A near-equilibrium crystal growth results from sluggish crystallisation kinetics driven by low undercooling, where cations are partitioned between clinopyroxene and melt according to thermodynamic principles. Similar near-equilibrium conditions were observed by Downes (1974) for sector-zoned titanaugite megacrysts
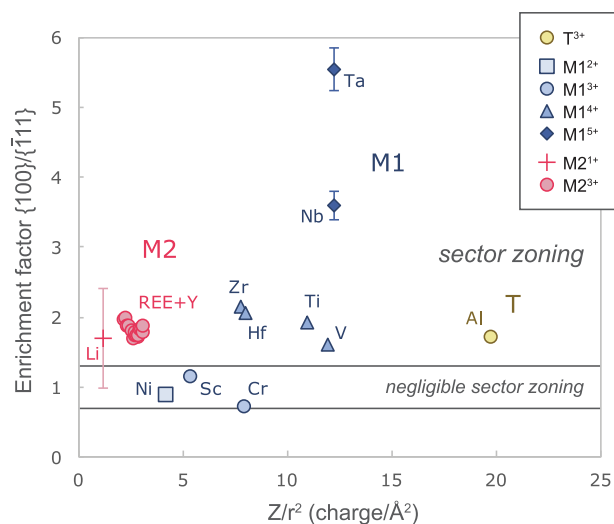

Fig. 7. Enrichment in minor and trace elements in sector {1 0 0} relative to sector {−1 1 1} of titanaugites 15RC018_Cpx1 and 15RC018_Cpx2, plotted as a function of ionic potential: ratio between the charge of the cation Z and the square of the radius of the cation r in IV-fold (T), VI-fold (M1) and VIII-fold (M2) coordination (plot after Shimizu, 1981; cation radii from Shannon, 1976). For simplicity, ionic potential is calculated for the primary cation site only, i.e., we consider the ionic radius of Al^{3+} in tetrahedral coordination and not in the octahedral M1 site. Note that for a given crystallographic site, the enrichment factor correlates positively with ionic potential and low-charge cations tend to show limited sector zoning (enrichment factor close to unity, within 1 ± 0.3). Uncertainties in enrichment factors were calculated from internal $2 \times$ standard errors on LA-ICP-MS data extracted for sectors {1 0 0} and {−1 1 1} (Supplementary Table 4); propagated uncertainties are smaller than symbols except for Li, Nb and Ta.

from Mt. Etna and by Kouchi et al. (1983) for experimental clinopyroxenes grown at low degrees of undercooling of $\Delta T = 13$–18 °C. Under such circumstances, the crystallisation kinetics lead to enrichments in incompatible cations in the order {1 0 0} > {1 1 0} > {0 1 0} > {−1 1 1} and opposite sector growth rates of {−1 1 1} > {0 1 0} > {1 1 0} > {1 0 0}. At higher degrees of undercooling ($\Delta T > 25$–45 °C), Kouchi et al. (1983) documented the development of hopper to dendritic morphologies where precise chemical correlations amongst sectors were hampered by strong disequilibrium effects.

In Etnean clinopyroxenes, the sector zoning generates marked compositional contrasts between the hourglass {−1 1 1} basal sectors and the {0 1 0}, {1 1 0} and {1 0 0} prism sectors (Figs. 2–6). Whilst differences amongst prism sectors are comparatively small, major cation exchanges between {−1 1 1} and {1 0 0} end-members can be expressed as:

$$[Si^{4+} + Mg^{2+} + Fe^{2+}]_{-111} \leftrightarrow [Al^{3+} + Ti^{4+} + Fe^{3+}]_{100} \quad (1)$$
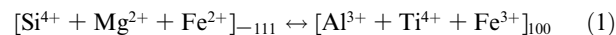
According to Nakamura (1973) and Dowty (1976), all sectors are characterised by an identical three-dimensional atomic configuration, but the surface of each individual growing sector has a specific two-dimensional atomic
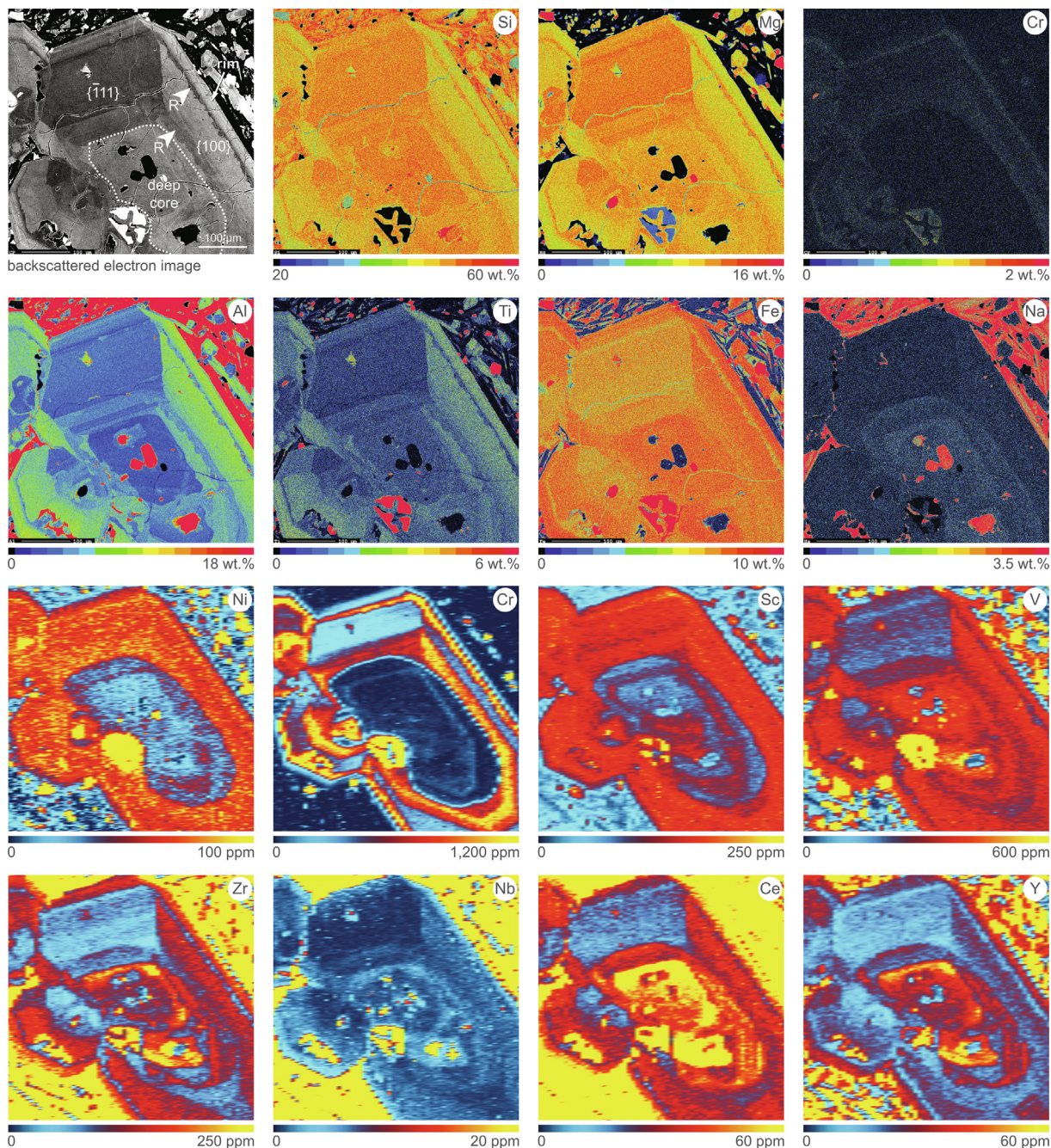
Fig. 8. Major and trace element maps of titanaugite 15RC004_Cpx1, obtained by electron microprobe (top two rows) and LA-ICP-MS (bottom two rows). The back-scattered electron image provides context. The crystal belongs to a glomerocryst set in a hypocrystalline groundmass. It represents an oblique cut of the crystal, between sections B and D in Fig. 1b. The crystal has a Na-rich anhedral (recycled) core. The mantle is sector-zoned and includes two Cr-rich recharge zones 'R' (white arrows). Note that the sharpness of the Cr map obtained by LA-ICP-MS (centre left; 3 h of analysis to map 12 elements) compared to that obtained by electron microprobe (top right corner; 16 h of analysis to map 5 elements). The crystal has a final Cr-poor, Al-Ti-rich rim.

arrangement. On the one hand, the geometry of the structural sites on the slow-growing {1 0 0} sector includes alternating layers of M and T sites that are not exposed simultaneously. The accretion of the T layer reduces the number of Si atoms available in the melt next to the crystal surface, favouring incorporation of Al in tetrahedral coordination (Hollister and Gancarz, 1971; Ferguson, 1973; Nakamura, 1973; Leung, 1974; Dowty, 1976; Skulski

et al., 1994). Meanwhile, a large number of divalent cations is required to fill layers composed entirely of M1 and M2 sites, promoting preferential incorporation of highly charged and relatively small cations such as Ti. Charge balance mechanisms thus involve $Si^{4+} \leftrightarrow Al^{3+}$ substitution in the tetrahedral site coupled with $Mg^{2+} + Fe^{2+} \leftrightarrow Ti^{4+} + Fe^{3+}$ exchange in octahedral sites (Mollo et al., 2018 and references therein). On the other hand, in the fast-growing

{−1 1 1} sector M and T sites are exposed simultaneously, thus limiting the incorporation of incompatible cations in tetrahedral and octahedral sites.

HFSE and REE are systematically accommodated in the octahedral sites of the clinopyroxene lattice to balance the charge deficiency caused by the increasing concentration of ^{T}Al (total Al per formula unit). In terms of clinopyroxene components and trace element partitioning, Eq. (1) can be reappraised as (Mollo et al., 2018 and references therein):

$$[DiHd]_{-111} \leftrightarrow [HFSETs + REETs]_{100} \qquad (2)$$

where DiHd = $CaMgSi_2O_6$ + $CaFeSi_2O_6$, and Ts = $CaAl_2$-SiO_6 + $CaFeSiAlO_6$. Therefore, the achievement of charge-neutral local configurations is the key mechanism driving trace element partitioning, as supported by the sympathetic relationship between sector zoning and ionic potential (Shimizu, 1981; Fig. 7). In other words, sector zoning of a cation reflects its ability to facilitate charge-balanced configurations. In the M1 octahedral site, HFSE and V^{4+} are strongly sector-zoned, even at very low concentrations (Fig. 4). Conversely, Cr^{3+} and Sc^{3+} show very minor sector variations and Ni^{2+} is not partitioned amongst sectors. Interestingly, Claeson et al. (2007) described marked sectoral differences for incompatible elements and constancy for transition metals, with the exception of vanadium. This element is very sensitive to the redox state of magma and has a valence of 4+ from quartz–fayalite–magnetite (QFM) to nickel-nickel oxide (NNO) buffering conditions (Mallmann and O'Neill, 2013), typical of Mt. Etna magmas (Armienti et al., 2013; Mollo et al., 2015). Preferential partitioning of V^{4+} into sectors supports the notion of charge-controlled partitioning. In turn, the role of ionic radius is evidenced by the sharp sector zoning of REE in the distorted (larger) M2 site (Figs. 4, 7), where only cations with charge lower than 3+ show limited sectoral variations (e.g., Ca^{2+} and Na^+ in Fig. 3). The geochemical behaviour of lithium agrees with this pattern (as a 1+ cation, it is not sector-zoned; Figs. 4, 7; Supplementary Fig. 1). It should be considered, however, that the fast chemical mobility of Li^+ (Costa and Morgan, 2011; Ellis et al., 2018) potentially leads to diffusive resetting of primary zoning in the course of magma storage, eruption and cooling.

Finally, it is worth stressing that the continuous growth of clinopyroxene sectors is compromised by occasional recharge events evidenced by high-Cr zones (Figs. 2, 5, 8). The irregular to wavy dissolution surfaces and slight kinks in inter-sectoral angles suggest abrupt changes in the physicochemical state of the system, in response to the arrival of hot magma characterised by a more primitive trace element composition (Streck, 2008; Ubide and Kamber, 2018).

4.2. Clinopyroxene-melt equilibrium and thermobarometry on sector-zoned crystals

To test the attainment of chemical equilibrium between the different sectors of clinopyroxene and the host magma and estimate P-T conditions of crystallisation, we combined mineral major elements with the bulk composition of the 1974 eccentric eruption (representative trachybasaltic scoria 160274FLA from Corsaro et al., 2009). Unlike common Etnean lavas, which usually contain a high proportion of phenocrysts (on average 25 vol.%; Corsaro et al., 2009), the 1974 eccentric eruption emitted nearly aphyric products (<5 vol.% phenocrysts) that can be considered as true liquid compositions.

A variety of mineral-melt equilibrium tests (Fig. 9a and b) indicate chemical equilibrium between clinopyroxene sectors and the melt. Considering the Fe-Mg exchange (Fig. 9a), refined at the equilibrium range of $Kd_{Fe-Mg}^{cpx-melt}$ = 0.28 ± 0.08 (Putirka, 2008), clinopyroxene data plot within or close to equilibrium with the melt. As expected from (Eq. (1)), the increase in Al from hourglass to prism sectors is followed by a decrease in Mg#, due to charge balance mechanisms enhancing coupled substitutions in {1 0 0} relative to {−1 1 1}. Such variation appears to prompt prism sectors partly away from Fe-Mg equilibrium. However, it has long been demonstrated that $Kd_{Fe-Mg}^{cpx-melt}$ is not a reliable indicator of clinopyroxene–melt equilibrium for a wide range of compositions (Putirka, 2008) and is not sensitive to kinetic effects on crystal growth (Mollo and Hammer, 2017). Instead, Mollo et al. (2013) proposed a more robust test for equilibrium based on the difference between diopside + hedenbergite (ΔDiHd) components predicted for clinopyroxene via global regression analysis of clinopyroxene-melt pairs in equilibrium conditions, and those measured in the analysed crystals (following the calculations in Putirka et al., 1996). The equilibrium condition is achieved when the value of ΔDiHd tends towards zero and clinopyroxene compositions plot on the one-to-one line of the 'DiHd measured' vs. 'DiHd predicted' diagram (Fig. 9b). The ΔDiHd test indicates that all clinopyroxene sectors studied here plot within the calibration error of the model (Fig. 9b). Additional models comparing measured and thermodynamically predicted partition coefficients for Na (D_{Na}; Blundy et al., 1995) and Ti (D_{Ti}; Hill et al., 2011; Mollo et al., 2018) at the estimated conditions of pressure and temperature (see below), further indicate equilibrium between all the sectors and the melt (Fig. 9b). This supports the interpretation that the crystal growth rate is slow and all clinopyroxene sectors remain in local chemical equilibrium with the melt feeding the advancing crystal surface.

Crystal cores show distinct Na_2O enrichments and relative CaO depletions compared to sector-zoned compositions (Fig. 6). However, the cores are not substantially different from the sectors in terms of major oxide composition (Fig. 6) and, thus, plot close to equilibrium with the 1974 melt (Fig. 9b). This implies that the crystal cores formed from a trachybasaltic magma similar in major element composition, but perhaps at different P-T conditions (e.g., Nimis, 1995). Finally, Al-Ti enrichments in the late-crystallising clinopyroxene rims (outermost rims) are typical of rapid growth under higher cooling rates. Therefore, the rims are deemed unsuitable for the application of thermobarometers as they lead to significant uncertainties (Mollo et al., 2013).

We explored the effect of sector zoning on P-T estimates by solving iteratively the pressure-independent, melt-
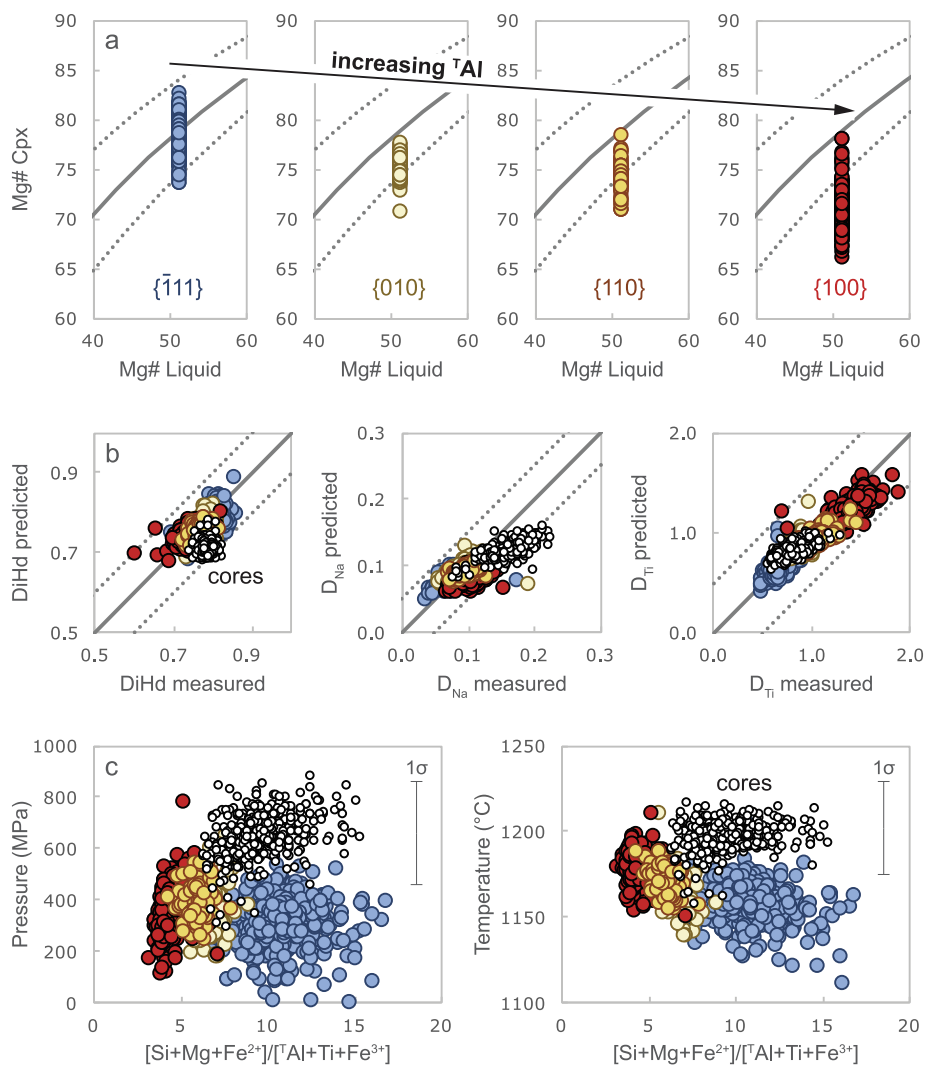
Fig. 9. Clinopyroxene-melt equilibrium and thermobarometry. (a) Test for Fe-Mg equilibrium between clinopyroxene sectors in the studied crystals and the 1974 melt (approached using the bulk chemistry of crystal-poor trachybasaltic scoria 160274FLA from Corsaro et al., 2009). Mg# = 100 Mg/(Mg + Fe), where concentrations are expressed on a molar basis. Many of the data plot within the accepted curves ($Kd_{Fe-Mg}^{cpx-melt}$ = 0.28 ± 0.08; Putirka, 2008), but Mg# in clinopyroxene prism sectors decreases below the equilibrium range as Al substitution increases (^{T}Al is total Al per formula unit). Note, however, that the fidelity of Fe-Mg exchange to indicate clinopyroxene-melt equilibrium is compromised because the value of $Kd_{Fe-Mg}^{cpx-melt}$ depends on melt composition (Putirka, 2008) and is not adequately sensitive to kinetic effects (Mollo et al., 2013; Mollo and Hammer, 2017). (b) Clinopyroxene-melt equilibrium tests comparing measured and predicted DiHd (Putirka et al., 1996; Mollo et al., 2013), D_{Na} (Blundy et al., 1995) and D_{Ti} (Hill et al., 2011; Mollo et al., 2018). Dashed lines encompass the calibration errors of the models. According to DiHd, D_{Na} and D_{Ti}, the vast majority of clinopyroxene data (recycled cores and sector-zoned mantles) are in equilibrium with the 1974 melt. (c) Pressure and temperature estimates for recycled cores and sector zones, plotted against the ratio between sums of cations enriched in the hourglass sectors (Si, Mg and Fe^{2+} atoms per formula unit) and in the prism sectors (^{T}Al, Ti and Fe^{3+} atoms per formula unit). Temperature estimates (T1 calibration, ±27 °C uncertainty; Putirka, 2008) were used as input data to calculate pressures (Cpx-only 32b calibration, ±200 MPa uncertainty; Putirka, 2008), which also consider the water content of the melt (2 wt.% H$_2$O; Armienti et al., 2007, 2013; Ubide and Kamber, 2018). Pressures and temperatures across sectors agree within error, whereas core compositions (small white circles with black border) suggest crystallisation at higher P-T conditions.

dependent thermometer T1 (±27 °C uncertainty; Putirka et al., 1996) and the temperature- and water-dependent, melt-independent barometer 32b (±200 MPa uncertainty; Putirka, 2008). Clinopyroxene-only barometers have provided reliable results at Etna and other alkaline systems, and are particularly useful when studying recycled parageneses (Ubide et al., 2014; Mollo et al., 2015; Hammer et al., 2016; Miller et al., 2017; Ubide and Kamber, 2018; Crossingham et al., 2018). Barometer 32b requires an esti-

mate of the water content of the melt, which was set at 2 wt.% to account for the hydrous nature of Etnean magmas (Armienti et al., 2007, 2013; Ubide and Kamber, 2018).

Compositional variations amongst sectors produce a mild gradient of P-T results from {−1 1 1} (lowest) to {1 0 0} (highest), however data overlap within uncertainty (Fig. 9c). On average, pressures vary from [310 ± 300 MPa]$_{-111}$ to [390 ± 250 MPa]$_{010}$ to [390 ± 250 MPa]$_{110}$ to [370 ± 300 MPa]$_{100}$, and temperatures

from $[1160 \pm 50 \,°C]_{\{-111\}}$ to $[1170 \pm 30 \,°C]_{\{010\}}$ to $[1170 \pm 20 \,°C]_{\{110\}}$ to $[1180 \pm 30 \,°C]_{\{100\}}$ (Fig. 9c). Considering the range of results and the error of estimate of the models, the P-T estimates of different sectors are virtually identical within the uncertainty. It follows that the sector zoning does not lead to significant errors in P-T estimates and therefore can be used to retrieve conditions of crystallisation.

Overall, P-T results are in agreement with previous thermobarometric constraints on Etnean clinopyroxene (Armienti et al., 2007, 2013; Mollo et al., 2015; Miller et al., 2017; Ubide and Kamber, 2018). Pressure estimates from sector compositions suggest crystallisation in the intermediate level plumbing system of Mt. Etna, where seismic and ground deformation data indicate magma storage regions located at 13–7, 8–9, 4–5, and 2 km (Murru and Montuori, 1999; Patanè et al., 2013). In contrast, the resorbed cores record crystallisation at higher P-T conditions of $1200 \pm 30 \,°C$ and 640 ± 300 MPa (Fig. 9c), close to the initial stage of clinopyroxene crystallisation near the Moho (Armienti et al., 2013; Ubide and Kamber, 2018).

The predictive power of both the T1 thermometer and the 32b barometer (Putirka, 2008) is mostly controlled by Na (jadeite) and Ca (diopside-hedenbergite) substitutions following volume changes in the crystal lattice (Nimis, 1995; Putirka, 2008). Distinct from the Na-rich and Ca-poor resorbed cores, the chemical gradients in Na and Ca across sectors are extremely low (Figs. 3, 6; Table 1). Hence, the cores predict distinct P-T conditions from the sector zones, but the different sectors are not resolvable from one another (Fig. 9c). The Na-Ca inter-sector constancy is in agreement with previous sector zoning studies on Etnean clinopyroxene (Downes, 1974; Duncan and Preston, 1980) and other volcanic systems globally (Hollister and Gancarz, 1971; Ferguson, 1973; Leung, 1974). In contrast, disequilibrium partitioning of Na into Al-Ti-rich sectors has been reported for clinopyroxenes from Aleutian (Brophy et al., 1999) and Hawaiian (Hammer et al., 2016; Welsch et al., 2016) basalts, where sector zoning was related to rapid crystal growth. Notably, the incorporation of REE in the clinopyroxene lattice is charge-balanced by either Al replacing Si in tetrahedral sites or Na replacing Ca in M2 sites (Mollo et al., 2018 and references therein). The lack of this latter substitution in Etnean clinopyroxenes can be interpreted as an indicator of sluggish crystallisation kinetics, leading to cation partitioning at near-equilibrium proportions under low degrees of undercooling. Indeed, at slow crystal growth rates, the fast-diffusing Na cations are more efficiently rejected away from the advancing crystal surface (Mollo and Hammer, 2017), with the consequence that P-T estimates are not significantly affected by sector zoning.

4.3. Modelling sector zoning trace element partitioning through the lattice strain theory

For a complete description and quantification of trace element incorporation in the $\{-1\,1\,1\}$ and $\{1\,0\,0\}$ sectors, we calculated apparent partition coefficients of HFSE (D_{HFSE}) and REE (D_{REE}) by dividing the composition of

each sector (Supplementary Table 5) by that of the host magma (assumed as the bulk rock analysis of sample 160274FLA from Corsaro et al., 2009; see Section 4.2). Furthermore, the same partition coefficients were modelled by employing a set of thermodynamically derived lattice strain equations (see Mollo et al., 2018 for further details), in which D_{HFSE} and D_{REE} are parameterised as a function of clinopyroxene chemistry (prevalently ^{T}Al) and the electrostatic effects emerging when the charge of the trace cation is different from the charge of the site-substituted major cation. This latter parameter has been recognised as one of the most important mechanisms controlling the incorporation of trace elements in the crystal lattice. For example, REE^{3+} cations enter the M2 site of typical charge 2+ leading to a net positive charge of 1+ and requiring that electrostatic work is done in placing the 'wrongly' charged cations into the crystallographic site (Wood and Blundy, 2001).

The apparent partition coefficients calculated for D_{Ti}-D_{Zr} and D_{Ce}-D_Y couples (as representative of D_{HFSE} and D_{REE}, respectively) closely match those modelled through the lattice strain approach (Fig. 10a), yielding a remarkably low average deviation for HFSE (0.16–0.19) and REE (0.04–0.06). It can be concluded that the partitioning of trace elements across the different sectors is driven by charge balance mechanisms operating at thermodynamic equilibrium. Therefore, the apparent partition coefficients for $\{-1\,1\,1\}$ and $\{1\,0\,0\}$ sectors are dependent on the lattice strain energy and thermodynamic principles, rather than on strong kinetic partitioning associated with disequilibrium cation incorporation (e.g., Mollo and Hammer, 2017).

Thermodynamic equilibrium is corroborated by the best-fit values derived for the strain-free partition coefficient (D_0) and their robust correlation ($R^2 = 0.97$–0.99) with ^{T}Al and the crystal electrostatic effects (Fig. 10b). Tetrahedral aluminium serves to increase D_{HFSE} and D_{REE} by increasing the charge-balanced configurations available to accommodate HFSE and REE in the M1 and M2 sites, respectively. Such configurations do not involve the electrostatic work of heterovalent substitutions, although the clinopyroxene structure is a complex solid solution with cation disorder on both tetrahedral and octahedral sites. As a consequence, locally in the crystal structure, charge-balanced configurations take place as heterovalent substitutions which are fulfilled by payment of an electrostatic energy penalty for size and charge mismatches. This penalty is quantified by the electrostatic work required to dissipate the excess (or deficit) charge on the specific crystal site, which translates into a significant control of crystal electrostatic effects on D_0 and trace element partitioning (Fig. 10b).

4.4. Implications for the interpretation of magma dynamics: A recipe for handling sector-zoned crystals

Sector zoning has been broadly documented in clinopyroxene from alkali basalts (Hollister and Gancarz, 1971; Ferguson, 1973; Wass, 1973; Leung, 1974; Downes, 1974; Duncan and Preston, 1980; Shimizu, 1981; Hammer et al., 2016; Welsch et al., 2016) and less commonly in
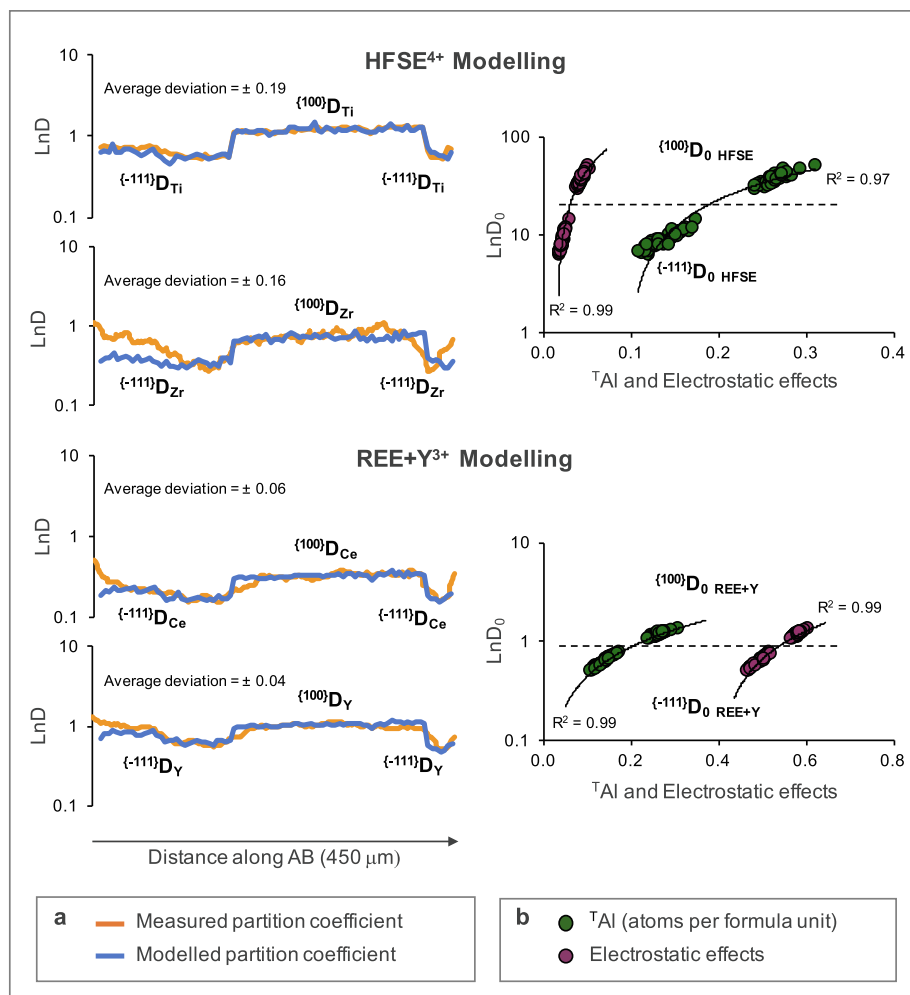
Fig. 10. Lattice strain modelling of sector zoning in titanaugite 15RC018_Cpx1. a) Measured vs. modelled partition coefficients for HFSE (D_{Ti}-D_{Zr}) and REE (D_{Ce}-D_Y) across the $\{-1\ 1\ 1\}$ and $\{1\ 0\ 0\}$ sectors, using data extracted from LA-ICP-MS maps (Fig. 4; Supplementary Table 5) and EPMA data (Fig. 3; Supplementary Table 2) along transect AB (Fig. 2). The values of HFSE and REE have been modelled through a set of thermodynamically derived lattice strain equations described in Mollo et al. (2018). (b) Dependence of the strain-free partition coefficient (D_0) on ^{T}Al and the crystal electrostatic effects. The values of D_0 have been derived through the regression fit of D_{HFSE} (Ti, Zr, Hf, Nb, Ta) and D_{REE} (14xREE and Y) groups. See more details in the text (Section 4.3).

tholeiitic systems (Nakamura, 1973; Neave and Putirka, 2017) and arc settings (Arculus, 1973; Brophy et al., 1999). However, the potential kinetic controls on mineral chemistry have undermined the utility of these crystals for the interpretation of magma histories. Indeed, compositional contrasts across sectors can be significant (e.g., Fig. 6; Table 1) and the identification of sectors themselves is challenging, particularly in regular thin section planes where crystals are exposed in random orientations. Therefore, the first step is to develop a comprehensive textural and compositional framework for the identification of hourglass and prism sectors (Fig. 1).

At Mt. Etna, polyhedral crystals with well-developed sector and concentric zonation (Figs. 2, 4) testify to slow, near-equilibrium growth. Crystallographic configurations enhance preferential incorporation of Al, HFSE and REE in the order: hourglass$_{\{-111\}}$ << prism$_{\{010\}}$ ≤ prism$_{\{110\}}$ < prism$_{\{100\}}$. The number of charge-balanced substitutions are minimised in $\{-1\ 1\ 1\}$, which is more reluctant to incorporate incompatible cations and might represent the most reliable recorder of 'true' equilibrium partitioning between the early-growing crystal surface and original magma composition (i.e., the bulk rock analysis). Nonetheless, the sluggishness of kinetic effects guarantees that local equilibrium is maintained persistently in terms of partitioning of major and trace element cations at the crystal-melt interface (Figs. 9b, 10). Consequently, for all sectors, the thermodynamic expressions that relate pressure and temperature variations to Jd-melt, Jd-DiHd and CaTs-DiHd equilibria, yield P-T estimates within the calibration errors of thermobarometers (Fig. 9c). In cases of faster growth, we infer that stronger kinetic effects might drive sectoral partitioning out of local thermodynamic equilibrium. For rapidly undercooled Etnean magmas in laboratory conditions (Mollo et al., 2013, 2018), Eq. (1) can be modified to the more general form:

$$[Si^{4+} + Mg^{2+} + Fe^{2+} + Ca^{2+}] \rightarrow [Al^{3+} + Ti^{4+} + Fe^{3+} + Na^+] \quad (3)$$
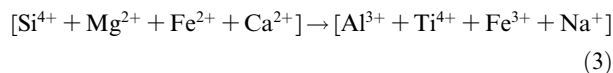
where increasing undercooling increases Al concentrations in clinopyroxene, leading to charge-balancing substitutions (moving from left to right in Eq. (3)). If our observations in natural sector zoned crystals are compared with the results from cooling experiments, the development of sector zoning, and even the extent of sector partitioning, may be used as an indicator of the degree of undercooling in the system. The transition from equilibrium crystallisation (no sector zoning) to near-equilibrium conditions (sector zoning following Eq. (1)) to disequilibrium effects (Eq. (3)) could reflect the development of increasing degrees of undercooling, for example at the margin of a reservoir or upon decompression (and volatile exsolution) during upward migration of magma (e.g., Brophy et al., 1999; Armienti et al., 2013). Thus, we propose that in vertical open systems, sector zoning might be explored as a proxy for magma ascent rate (Fig. 11).

In this study, crystal cores are non-sector-zoned and crystallised in storage regions at depth where long-term crystallisation processes take place (Mollo et al., 2015; Ubide and Kamber, 2018). The cores commonly show concentric or irregular compositional variations (Fig. 8), which rule out potential diffusive resetting of zoning over protracted storage at magmatic temperatures. Hence, it is plausible that the lack of sector zoning in cores is primary and related to equilibrium crystallisation. Sector-zoned crystals following Eq. (1) are common in Etnean monogenetic eruptions, some of which are fed by magma tapped rapidly from depth through eccentric pathways bypassing the central conduits of the volcano (Behncke and Neri, 2003; Clocchiatti et al., 2004; Corsaro et al., 2009; Ubide and Kamber, 2018; Fig. 11). Further, we speculate that under conditions of higher undercooling, increased kinetic effects may generate sector-zoned crystals that follow Eq. (3). It is unclear, however, if the order of sector partitioning would hold the hourglass-prism pattern observed at low undercooling (Eq. (1)) or change at increasing undercooling, as reported in the experimental work by Kouchi
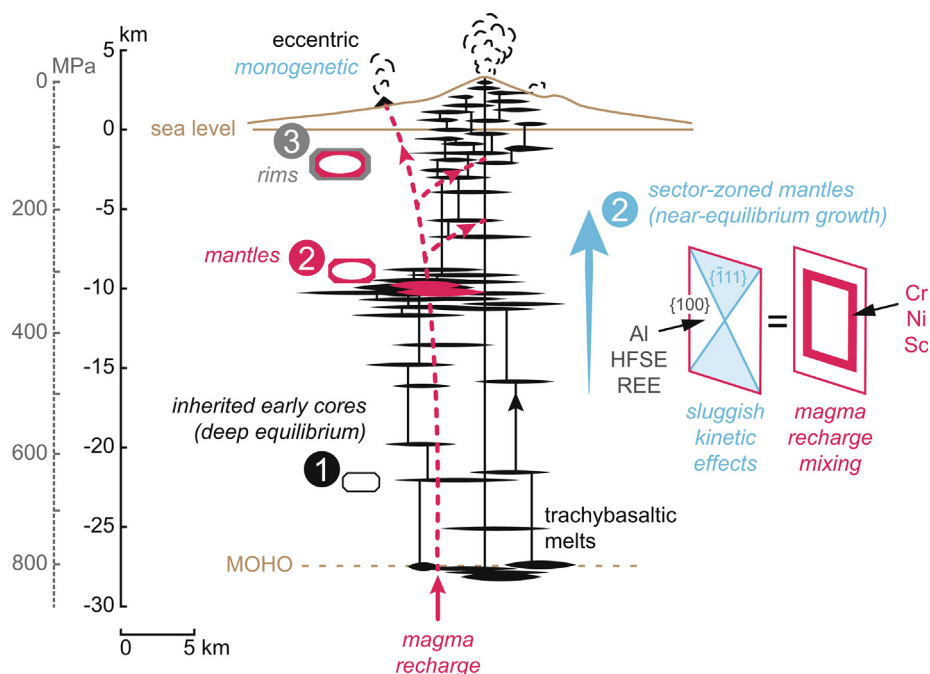

Fig. 11. Schematic model of the plumbing system feeding Mt. Etna (simplified from Ubide and Kamber, 2018), and development of sector-zoned clinopyroxene crystals under conditions of low undercooling and sluggish kinetics. We propose that magma stagnation leads to equilibrium crystallisation with no sector zoning (stages 1 and 2-pink), whereas near-equilibrium crystallisation at low undercooling may generate sector zoning (stage 2-blue). Such small thermal gradients may occur during slow magma ascent (stage 2-blue), or alternatively at the margin of a reservoir. Finally, magma ascent accelerates inducing rapid growth of rims and microcrysts/microlites (stage 3). Interestingly, dynamic crystallisation could be an identifying feature preceding rapid decompression along eccentric pathways, leading to monogenetic eruptions. In sector-zoned mantles, most major elements, HFSE and REE partition into sectors, and the incorporation of incompatible elements increases from the hourglass {−1 1 1} basal sector to the {0 1 0}, {1 1 0} and {1 0 0} prism sectors (Eqs. (1) and (2)). In contrast, Cr, Ni and, to a lesser extent, Sc, show little sector zoning (Fig. 7); instead, they show oscillatory zoning in response to mafic recharge. The reliability of low-charge transition metals as recorders of melt compositions makes it possible to reconstruct magmatic histories and investigate eruption triggers even in sector-zoned crystals. At Etna, the recharge magma recycles previous cores formed very slowly during magma stagnation at depth (ca. 650 MPa; Fig. 9c), showing no sector zoning and high Na contents (Figs. 6, 8). Crystal mantles can be either non-sector-zoned (equilibrium crystallisation during storage at ca. 10 km; Ubide and Kamber, 2018) or sector-zoned (dynamic crystallisation at low ascent rates from 500-200 MPa (Fig. 9c); low undercooling still imposes slow growth). Final rims crystallise upon fast decompression and degassing and have higher Al-Ti contents than the preceding mantle composition (Fig. 3). On the left-hand side, the depth scale is continuously linear whereas the pressure scale follows density changes across the crustal column (Corsaro and Pompilio, 2004). The Moho depth is at 27.4 km after Hirn et al. (1997). (For interpretation of the references to colour in this figure legend, the reader is referred to the web version of this article.)

et al. (1983). Reversals in sectoral partitioning as a function of ΔT were recently proposed in Hawaii, where sector-zoned clinopyroxenes are characterised by spongy textures, herald of strong disequilibrium processes (Hammer et al., 2016; Welsch et al., 2016). Finally, it should be considered that sector zonings might be dependent not only on growth rates and crystal structure but also on the composition of coexisting liquids (Nakamura, 1973; Kouchi et al., 1983). For example, clinopyroxenes from tholeiitic systems often display strong sector zoning in $Ca/(Ca + Mg + Fe)$ and mild positive correlations between Ca and Al (Nakamura, 1973; Neave and Putirka, 2017), in contrast with the strong Al-Ti-dominated partitioning observed in alkaline systems (e.g., Eq. (1)). Improving the inventory of sector zoning in natural and experimental systems with modern techniques holds promise to infer the rates of cooling and ascent in magmatic plumbing systems.

In terms of trace element partitioning, it is worth highlighting that Eq. (2) does not involve low-charge transition metals. In particular, low ionic potential Cr, Sc and Ni are poor advocates for charge balance and do not respond significantly to sector zoning. Enrichments in these elements, together with relative depletions in REE and HFSE, are good indicators of the injection and mixing of mafic magma into the system, particularly when they overgrow dissolution surfaces. This finding is relevant from petrological, volcanological and eruption hazards perspectives, given that the identification of mafic recharge events has proven crucial for the understanding of eruption triggering mechanisms and timescales in volcanic systems (Kent et al., 2010; Bouvet de Maisonneuve et al., 2016; Petrone et al., 2018; Ubide and Kamber, 2018).

5. CONCLUSIONS

We have investigated major and trace element compositional variations in sector-zoned clinopyroxene crystals from Mt. Etna in a spatial context. Our data confirm that sector zoning is controlled by (1) the crystallographic structure of the mineral and (2) its growth rate (typically related to the degree of magma undercooling). We find that:

- Sector-zoned crystals comprise two types of sectors: hourglass (or basal), and prism. The hourglass sectors are relatively enriched in Si-Mg compared to prism sectors, which incorporate increasing concentrations of Al, HFSE and REE. At Mt. Etna, enrichment in Al-HFSE-REE follows the order: $hourglass_{\{-111\}} \ll prism_{\{010\}} \leq prism_{\{110\}} < prism_{\{100\}}$.
- Kinetic effects have a large influence on the incorporation of HFSE and REE, which show strong sector zoning. In contrast, cations with low charge relative to the radius of the crystallographic site they occupy do not show significant sectoral partitioning.
- Coupled enrichments in compatible low-charge transition metals Cr-Ni-(Sc) and depletions in incompatible HFSE and REE along concentric zones, particularly overgrowing resorbed cores, are excellent recorders of mafic replenishment and magma mixing at depth, even in sector-zoned crystals.

- Sector zoning can develop under near-equilibrium conditions at relatively low degrees of undercooling and slow growth rates. In such circumstances, sector-zoned clinopyroxene can be explored for the application of thermobarometric models due to the effects of sluggish crystallisation kinetics.
- The low degree of undercooling inferred for the development of sectoral partitioning implies that the presence of sector-zoned crystals may provide insights into magma ascent and cooling history.

This study aims to expand the interest of the petrological community in sector zoning, offering a reappraisal of major and trace element incorporation mechanisms during the growth of clinopyroxene in dynamic environments. We expect that the outcome of this study will help shift the conventional prejudice on sector-zoned crystals towards a new approach of investigating equilibrium conditions and elemental variations that can still provide reliable constraints and insight to decipher magma history and P-T conditions of crystallisation.

APPENDIX A. SUPPLEMENTARY MATERIAL

Supplementary data to this article can be found online at https://doi.org/10.1016/j.gca.2019.02.021.

REFERENCES

Andronico D., Branca S., Calvari S., Burton M., Caltabiano T., Corsaro A. R., Del Carlo P., Garfi G., Lodato L., Miraglia L., Murè F., Neri M., Pecora E., Pompilio M., Salerno G. and Spampinato L. (2005) A multi-disciplinary study of the 2002–03 Etna eruption: insights into a complex plumbing system. *Bull. Volcanol.* **67**, 314–330. https://doi.org/10.1007/s00445-004-0372-8.

Arculus R. J. (1973) *The alkali fasalt, andesite association of grenada, lesser antilles* PhD Thesis. Durham University.

Armienti P., Tonarini S., Innocenti F. and D'Orazio M. (2007) Mount Etna pyroxene as tracer of petrogenetic processes and dynamics of the feeding system. *Geol. Soc. Am. Spec. Pap.* **418**, 265–276. https://doi.org/10.1130/2007.2418(13).

Armienti P., Perinelli C. and Putirka K. D. (2013) A new model to estimate deep-level magma ascent rates, with applications to

Mt. Etna (Sicily, Italy). *J. Petrol.* **54**, 795–813. https://doi.org/10.1093/petrology/egs085.

Behncke B. and Neri M. (2003) The July–August 2001 eruption of Mt. Etna (Sicily). *Bull. Volcanol.* **65**, 461–476. https://doi.org/10.1007/s00445-003-0274-1.

Blundy J. D., Falloon T. J., Wood B. J. and Dalton J. A. (1995) Sodium partitioning between clinopyroxene and silicate melts. *J. Geophys. Res. Solid Earth* **100**, 15501–15515. https://doi.org/10.1029/95JB00954.

Bouvet de Maisonneuve C., Costa F., Huber C., Vonlanthen P., Bachmann O. and Dungan M. A. (2016) How do olivines record magmatic events? Insights from major and trace element zoning. *Contrib. Mineral. Petrol.* **171**, 56. https://doi.org/10.1007/s00410-016-1264-6.

Brophy J. G., Whittington C. S. and Park Y. R. (1999) Sector-zoned augite megacrysts in Aleutian high alumina basalts: implications for the conditions of basalt crystallization and the generation of calc-alkaline series magmas. *Contrib. Mineral. Petrol.* **135**, 277–290.

Claeson D. T., Meurer W. P., Hogmalm K. J. and Larson S. Å. (2007) Using LA-ICPMS mapping and sector zonation to understand growth and trace-element partitioning in sector-zoned clinopyroxene oikocrysts from the Norra Ulvö gabbro, Sweden. *J. Petrol.* **48**, 711–728. https://doi.org/10.1093/petrology/egl079.

Clocchiatti R., Condomines M., Guénot N. and Tanguy J. C. (2004) Magma changes at Mount Etna: the 2001 and 2002–2003 eruptions. *Earth Planet. Sci. Lett.* **226**, 397–414. https://doi.org/10.1016/j.epsl.2004.07.039.

Corsaro R. A. and Pompilio M. (2004) Buoyancy-controlled eruption of magmas at Mount Etna. *Terra Nova* **16**, 16–22.

Corsaro R. A., Métrich N., Allard P., Andronico D., Miraglia L. and Fourmentraux C. (2009) The 1974 flank eruption of Mount Etna: an archetype for deep dike-fed eruptions at basaltic volcanoes and a milestone in Etna's recent history. *J. Geophys. Res.* **114**, B07204. https://doi.org/10.1029/2008JB006013.

Costa F. and Morgan D. (2011) Time constraints from chemical equilibration in magmatic crystals. In *Timescales of Magmatic Processes: From Core to Atmosphere* (eds. A. Dosseto, S. P. Turner and J. A. Van Orman). Blackwell Publishing Ltd..

Crossingham T. J., Ubide T., Vasconcelos P. M. and Mallmann G. (2018) Parallel plumbing systems feeding a pair of coeval volcanoes in eastern Australia. *J. Petrol.* **59**, 1035–1066.

D'Orazio M., Armienti P. and Cerretini S. (1998) Phenocryst/matrix trace-element partition coefficients for hawaiite-trachyte lavas from the Ellittico volcanic sequence (Mt. Etna, Sicily, Italy). *Mineral. Petrol.* **64**, 65–68.

Davidson J. P., Morgan D. J., Charlier B. L. A., Harlou R. and Hora J. M. (2007) Microsampling and isotopic analysis of igneous rocks: implications for the study of magmatic systems. *Ann. Rev. Earth Planet. Sci.* **35**, 273–311. https://doi.org/10.1146/annurev.earth.35.031306.140211.

Downes M. J. (1974) Sector and oscillatory zoning in calcic augites from M. Etna, Sicily. *Contrib. Mineral. Petrol.* **47**, 187–196.

Dowty E. (1976) Crystal structure and crystal growth: II. Sector zoning in minerals. *Am. Mineral.* **61**, 460–469.

Droop G. T. R. (1987) A general equation for estimating Fe3+ concentrations in ferromagnesian silicates and oxides from microprobe analyses, using stoichiometric criteria. *Min. Mag.* **51**, 431–435.

Duncan A. M. and Preston R. M. F. (1980) Chemical variation of clinopyroxene phenocrysts from the trachybasaltic lavas of Mount Etna, Sicily. *Min. Mag.* **43**, 765–770.

Ellis B. S., Szymanowski D., Magna T., Neukampf J., Dohmen R., Bachmann O., Ulmer P. and Guillong M. (2018) Post-eruptive mobility of lithium in volcanic rocks. *Nat. Commun.* **9**, 3228. https://doi.org/10.1038/s41467-018-05688-2.

Ferguson A. K. (1973) On hour-glass sector zoning in clinopyroxene. *Min. Mag.* **39**, 321–325.

Ganne J., Bachmann O. and Feng X. (2018) Deep into magma plumbing systems: interrogating the crystal cargo of volcanic deposits. *Geology* **2018133**. https://doi.org/10.1130/G39857.1.

Hammer J., Jacob S., Welsch B., Hellebrand E. and Sinton J. (2016) Clinopyroxene in postshield Haleakala ankaramite: 1. Efficacy of thermobarometry. *Contrib. Mineral. Petrol.* **171**, 7. https://doi.org/10.1007/s00410-015-1212-x.

Hart S. R. and Dunn T. (1993) Experimental cpx/melt partitioning of 24 trace elements. *Contrib. Mineral. Petrol.* **113**, 1–8.

Hill E., Blundy J. D. and Wood B. J. (2011) Clinopyroxene-melt trace element partitioning and the development of a predictive model for HFSE and Sc. *Contrib. Mineral. Petrol.* **161**, 423–438. https://doi.org/10.1007/s00410-010-0540-0.

Hirn A., Nicolich R., Gallart J., Laigle M., Cernobori L. and ETNASEIS Scientific Group (1997) Roots of Etna volcano in faults of great earthquakes. *Earth Planet. Sci. Lett.* **148**, 171–191.

Hollister L. S. and Gancarz A. J. (1971) Compositional sector-zoning in clinopyroxene from the Narce area, Italy. *Am. Mineral.* **56**, 959–979.

Jarosewich E., Nelen J. A. and Norberg J. A. (1980) Reference samples for electron microprobe analysis. *Geostandards Newsletter* **4**, 43–47.

Kent A. J. R., Darr C., Koleszar A. M., Salisbury M. J. and Cooper K. M. (2010) Preferential eruption of andesitic magmas through recharge filtering. *Nat. Geosci.* **3**, 631–636. https://doi.org/10.1038/NGEO924.

Kouchi A., Sugawara Y., Kashima K. and Sunagawa I. (1983) Laboratory growth of sector zoned clinopyroxenes in the system CaMgSi2O6 – CaTiAl2O6. *Contrib. Mineral. Petrol.* **83**, 177–184.

Leung I. S. (1974) Sector-zoned titanaugites: morphology, crystal chemistry, and growth. *Am. Mineral.* **59**, 127–138.

Lofgren G. E., Huss G. R. and Wasserburg G. J. (2006) An experimental study of trace-element partitioning between Ti-Al-clinopyroxene and melt: equilibrium and kinetic effects including sector zoning. *Am. Mineral.* **91**, 1596–1606. https://doi.org/10.2138/am.2006.2108.

Longerich H. P., Jackson S. E. and Günther D. (1996) Laser ablation inductively coupled plasma mass spectrometric transient signal data acquisition and analyte concentration calculation. *J. Anal. At. Spectrom.* **11**, 899–904.

Mallmann G. and O'Neill H. (2013) Calibration of an empirical thermometer and oxybarometer based on the partitioning of Sc, Y and V between olivine and silicate melt. *J. Petrol.* **54**, 933–949. https://doi.org/10.1093/petrology/egt001.

Métrich N., Allard P., Spilliaert N., Andronico D. and Burton M. (2004) 2001 flank eruption of the alkali- and volatile-rich primitive basalt responsible for Mount Etna's evolution in the last three decades. *Earth Planet. Sci. Lett.* **228**, 1–17. https://doi.org/10.1016/j.epsl.2004.09.036.

Miller S. A., Myers M., Fahnestock M. F., Bryce J. G. and Blichert-Toft J. (2017) Magma dynamics of ancient Mt. Etna inferred from clinopyroxene isotopic and trace element systematics. *Geochem. Perspect. Lett.* **4**, 47–52.

Mollo S. and Hammer J. (2017) Dynamic crystallization in magmas. *EMU Notes Mineral.* **16**, 373–418. https://doi.org/10.1180/EMU-notes.16.12.

Mollo S., Blundy J. D., Iezzi G., Scarlato P. and Langone A. (2013) The partitioning of trace elements between clinopyroxene and trachybasaltic melt during rapid cooling and crystal growth. *Contrib. Mineral. Petrol.* **166**, 1633–1654. https://doi.org/10.1007/s00410-013-0946-6.

Mollo S., Giacomoni P. P., Coltorti M., Ferlito C., Iezzi G. and Scarlato P. (2015) Reconstruction of magmatic variables governing recent Etnean eruptions: constraints from mineral

chemistry and P-T–fO2–H2O modelling. *Lithos* **212–215**, 311–320. https://doi.org/10.1016/j.lithos.2014.11.020.

Mollo S., Blundy J., Scarlato P., De Cristofaro S. P., Tecchiato V., Di Stefano F., Vetere F., Holtz F. and Bachmann O. (2018) An integrated P-T-H2O-lattice strain model to quantify the role of clinopyroxene fractionation on REE+Y and HFSE patterns of mafic alkaline magmas: application to eruptions at Mt. Etna. *Earth Sci. Rev.* **185**, 32–56. https://doi.org/10.1016/j.earscirev.2018.05.014.

Morimoto N., Fabries J., Ferguson A. K., Ginzburg I. V., Ross M., Seifert F. A., Zussman J., Aoki K. and Gottardi G. (1988) Nomenclature of pyroxenes. *Mineral. Mag.* **52**, 535–550.

Müller T., Dohmen R., Becker H. W., Ter Heege J. H. and Chakraborty S. (2013) Fe–Mg interdiffusion rates in clinopyroxene: experimental data and implications for Fe–Mg exchange geothermometers. *Contrib. Mineral. Petrol.* **166**, 1563–16576. https://doi.org/10.1007/s00410-013-0941-y.

Murru M. and Montuori C. (1999) The locations of magma chambers at Mt. Etna, Italy, mapped by b-values. *Geophys. Res. Lett.* **26**, 2553–2556.

Nakamura Y. (1973) Origin of sector-zoning of igneous clinopyroxenes. *Am. Mineral.* **58**, 986–990.

Nakagawa M., Wada K. and Wood C. P. (2002) Mixed magmas, mush chambers and eruption triggers: evidence from zoned clinopyroxene phenocrysts in andesitic scoria from the 1995 eruptions of Ruapehu volcano, New Zealand. *J. Petrol.* **43**, 2279–2303.

Neave D. A. and Putirka K. D. (2017) A new clinopyroxene-liquid barometer, and implications for magma storage pressures under Icelandic rift zones. *Am. Mineral.* **102**, 777–794. https://doi.org/10.2138/am-2017-5968.

Nimis P. (1995) A clinopyroxene geobarometer for basaltic systems based on crystals-structure modeling. *Contrib. Mineral. Petrol.* **121**, 115–125.

Patanè D., Aiuppa A., Aloisi M., Behncke B., Cannata A., Coltelli M., Di Grazia G., Gambino S., Gurrieri S., Mattia M. and Salerno G. (2013) Insights into magma and fluid transfer at Mount Etna by a multiparametric approach: a model of the events leading to the 2011 eruptive cycle. *J. Geophys. Res. Solid Earth* **118**, 3519–3539. https://doi.org/10.1002/jgrb.50248.

Paton C., Hellstrom J., Paul B., Woodhead J. and Hergt J. (2011) Iolite: freeware for the visualisation and processing of mass spectrometric data. *J. Anal. At. Spectrom.* **26**, 2508–2518. https://doi.org/10.1039/c1ja10172b.

Paul B., Paton C., Norris A., Woodhead J., Hellstrom J., Hergt J. and Greig A. (2012) Cell Space: a module for creating spatially registered laser ablation images within the Iolite freeware environment. *J. Anal. At. Spectrom.* **27**, 700–706. https://doi.org/10.1039/c2ja10383d.

Perinelli C., Mollo S., Gaeta M., De Cristofaro S. P., Palladino D. M., Armienti P., Scarlato P. and Putirka K. D. (2016) An improved clinopyroxene-based hygrometer for Etnean magmas and implications for eruption triggering mechanisms. *Am. Mineral.* **101**, 2774–2777. https://doi.org/10.2138/am-2016-5916.

Petrone C. M., Braschi E., Francalanci L., Casalini M. and Tommasini S. (2018) Rapid mixing and short storage timescale in the magma dynamics of a steady-state volcano. *Earth Planet. Sci. Lett.* **492**, 206–221. https://doi.org/10.1016/j.epsl.2018.03.055.

Petrus J. A., Chew D. M., Leybourne M. I. and Kamber B. S. (2017) A new approach to laser-ablation inductively-coupled-plasma mass spectrometry (LA-ICP-MS) using the flexible map interrogation tool 'Monocle'. *Chem. Geol.* **463**, 76–93. https://doi.org/10.1016/j.chemgeo.2017.04.027.

Putirka K. D., Johnson M., Kinzler R. J., Longhi J. and Walker D. (1996) Thermobarometry of mafic igneous rocks based on clinopyroxene-liquid equilibria, 0–30 kbar. *Contrib. Mineral. Petrol.* **123**, 92–108.

Putirka K. D. (2008) Thermometers and barometers for volcanic systems. *Rev. Mineral. Geochem.* **69**, 61–120.

Schwandt C. S. and McKay G. A. (2006) Minor- and trace-element sector zoning in synthetic enstatite. *Am. Mineral.* **91**, 1607–1615. https://doi.org/10.2138/am.2006.2093.

Shannon R. D. (1976) Revised effective ionic-radii and systematic studies of interatomic distances in halides and chalcogenides. *Acta Crystallogr. A* **32**, 751–767.

Shimizu N. (1981) Trace element incorporation into growing augite phenocryst. *Nature* **289**, 575–577.

Skulski T., Minarik W. and Watson E. B. (1994) High-pressure experimental trace-element partitioning between clinopyroxene and basaltic melts. *Chem. Geol.* **117**, 127–147.

Stock M. J., Bagnardi M., Neave D. A., Maclennan J., Bernard B., Buisman I., Gleeson M. L. M. and Geist D. (2018) Integrated petrological and geophysical constraints on magma system architecture in the western Galápagos Archipelago: insights from Wolf volcano. *Geochem., Geophys., Geosyst.* **19**. https://doi.org/10.1029/2018GC007936.

Streck M. J. (2008) Mineral textures and zoning as evidence for open system processes. *Rev. Mineral. Geochem.* **69**, 595–622.

Tanguy J. C. and Kieffer G. (1976) The 1974 eruption of Mount Etna. *Bull. Volcanol.* **40**(4), 239–252.

Ubide T. and Kamber B. S. (2018) Volcanic crystals as time capsules of eruption history. *Nature Commun.* **9**, 326. https://doi.org/10.1038/s41467-017-02274-w.

Ubide T., Galé C., Arranz E., Lago M. and Larrea P. (2014) Clinopyroxene and amphibole crystal populations in a lamprophyre sill from the Catalonian Coastal Ranges (NE Spain): a record of magma history and a window to mineral-melt partitioning. *Lithos* **184–187**, 225–242. https://doi.org/10.1016/j.lithos.2013.10.029.

Ubide T., McKenna C. A., Chew D. M. and Kamber B. S. (2015) High-resolution LA-ICP-MS trace element mapping of igneous minerals: in search of magma histories. *Chem. Geol.* **409**, 157–168. https://doi.org/10.1016/j.chemgeo.2015.05.020.

Van Orman J. A., Grove T. L. and Shimizu N. (2001) Rare earth element diffusion in diopside: influence of temperature, pressure, and ionic radius, and an elastic model for diffusion in silicates. *Contrib. Mineral. Petrol.* **141**, 687–703. https://doi.org/10.1007/s004100100269.

Wass S. Y. (1973) The origin and petrogenetic significance of hourglass zoning in titaniferous clinopyroxenes. *Min. Mag.* **39**, 133–144.

Watson E. B. and Liang Y. (1995) A simple model for sector zoning in slowly grown crystals: Implications for growth rate and lattice diffusion, with emphasis on accessory minerals in crustal rocks. *Am. Mineral.* **80**, 1179–1187.

Welsch B., Hammer J., Baronnet A., Jacob S., Hellebrand E. and Sinton J. (2016) Clinopyroxene in postshield Haleakala ankaramite: 2. Texture, compositional zoning and supersaturation in the magma. *Contrib. Mineral. Petrol.* **171**, 6. https://doi.org/10.1007/s00410-015-1213-9.

Wood B. J. and Blundy J. D. (2001) The effect of cation charge on crystal–melt partitioning of trace elements. *Earth Planet. Sci. Lett.* **188**, 59–71. https://doi.org/10.1016/S0012-821X(01)00294-1.

Wood B. J. and Blundy J. D. (2003) Trace element partitioning under crustal and uppermost mantle conditions: the influences of ionic radius, cation charge, pressure, and temperature. In *Treatise on Geochemistry*, vol. 1 (ed. A. M. Davis). Elsevier, pp. 395–424.

Associate editor: Rosemary Hickey-Vargas